

IMPLICIT METHODS FOR EQUATION-FREE ANALYSIS: CONVERGENCE RESULTS AND ANALYSIS OF EMERGENT WAVES IN MICROSCOPIC TRAFFIC MODELS

CHRISTIAN MARSCHLER*, JAN SIEBER†, RAINER BERKEMER‡, ATSUSHI
KAWAMOTO§, AND JENS STARKE¶

Abstract. We introduce a general formulation for an implicit equation-free method in the setting of slow-fast systems. First, we give a rigorous convergence result for equation-free analysis showing that the implicitly defined coarse-level time stepper converges to the true dynamics on the slow manifold within an error that is exponentially small with respect to the small parameter measuring time scale separation. Second, we apply this result to the idealized traffic modeling problem of phantom jams generated by cars with uniform behavior on a circular road. The traffic jams are waves that travel slowly against the direction of traffic. Equation-free analysis enables us to investigate the behavior of the microscopic traffic model on a macroscopic level. The standard deviation of cars' headways is chosen as the macroscopic measure of the underlying dynamics such that traveling wave solutions correspond to equilibria on the macroscopic level in the equation-free setup. The collapse of the traffic jam to the free flow then corresponds to a saddle-node bifurcation of this macroscopic equilibrium. We continue this bifurcation in two parameters using equation-free analysis.

Key words. equation-free methods, implicit methods, lifting, traffic modeling, optimal velocity model, traveling waves, stability of traffic jams

AMS subject classifications. 65P30, 37M20, 37Mxx, 34E13

1. Introduction. When one studies systems with many degrees of freedom, for example, systems with a large number of particles or interacting agents, one is often interested not so much in the trajectories at the microscopic level (that is, of individual particles), but in the behavior on the macroscopic scale (of the overall distribution of particles). The classical example is the motion of molecules of a gas, resulting in the laws of thermodynamics. In this classical case the macroscopic description is derived in statistical mechanics from knowledge about the microscopic behavior through time scale separation. Other important examples are emerging patterns in physical, chemical, and biological systems, e.g., Rayleigh-Bénard convection rolls [32], the Belousov-Zhabotinsky reaction [3, 44], and stripes on zebra skin or patterns on butterfly wings [41]. A common approach in the physics literature to deriving macroscopic descriptions are the so-called adiabatic elimination or the slaving principle [15, 16]. These concepts are related to the theorems in the mathematical literature about reductions to center manifolds or slow manifolds [7, 20, 40].

For systems where no explicit macroscopic description can be derived from microscopic models, Kevrekidis and coworkers proposed that, if the number of particles is moderate, then it is sometimes possible to skip the derivation of a macroscopic description by performing the analysis of the dynamics in the macroscopic scale directly.

*Department of Mathematics, Technical University of Denmark, Matematiktorvet 303B, DK-2800 Kgs. Lyngby, Denmark (c.marschler@mat.dtu.dk).

†College of Engineering, Mathematics and Physical Sciences, University of Exeter, North Park Road, Exeter (Devon) EX4 4QF (j.sieber@exeter.ac.uk).

‡AKAD University of Applied Sciences, Maybachstrasse 18-20, D-70469 Stuttgart, Germany (rainer.berkemer@akad.de).

§Toyota Central R&D Labs., Inc., Nagakute, Aichi 480-1192, Japan (atskwmt@mosk.tytlabs.co.jp).

¶Department of Mathematics, Technical University of Denmark, Matematiktorvet 303B, DK-2800 Kgs. Lyngby, Denmark (j.starke@mat.dtu.dk).

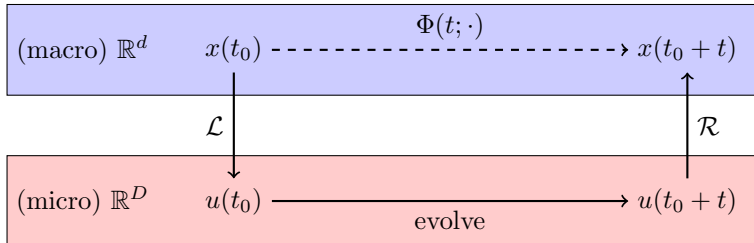


FIG. 1.1. Sketch of the macroscopic time stepper $\Phi(t; \cdot)$. The macroscopic state $x(t_0)$ is mapped to a microscopic state $u(t_0)$ by using the lifting operator \mathcal{L} . The available microscopic time stepper is used to evolve the system to the microscopic state $u(t_0 + t)$, which is mapped to a macroscopic state $x(t_0 + t)$ using the restriction operator \mathcal{R} . This procedure constitutes the coarse-level time stepper $\Phi(t; \cdot)$.

This approach relies on evaluating short bursts of appropriately initialized simulations of the microscopic model (see, for example, [22, 23, 24] for recent reviews). It is called *equation-free* because it assumes that the macroscopic model exists but is not available as an explicit formula. Equation-free methods are particularly appealing if either explicit macroscopic descriptions are unavailable, or one wants to study the underlying system near the boundary of validity of its macroscopic description (for example, as one decreases the number of particles, finite size effects may start to appear as small corrections to the macroscopic model). Equation-free analysis has been applied for a large class of multiscale models that roughly fit the description of *singularly perturbed systems* [9] in a broad sense (see motivation in [24]), such as stochastic systems [28, 37], agent-based models [5, 6, 14], molecular dynamics [4] or neural dynamics [26, 33], to perform high-level tasks such as bifurcation analysis, optimization or control design [8, 36].

The basic building block of equation-free analysis is an approximate coarse-level time stepper $\Phi(t; \cdot)$ for short times t (compared to the slow time scale) in the phase space of macroscopic variables (say, \mathbb{R}^d). This coarse-level time stepper is typically composed of three steps: *lift* (operator \mathcal{L}), *evolve*, and *restrict* (operator \mathcal{R}), as shown in Figure 1.1. To compute the map $\Phi(t; x)$ on a given macroscopic state $x \in \mathbb{R}^d$, one has to apply a lifting operator \mathcal{L} to map x to a microscopic state $u \in \mathbb{R}^D$ (typically, $D \gg d$); then one runs the microscopic simulation for the time t ; and finally one maps the end state of the microscopic simulation back into \mathbb{R}^d using a restriction operator \mathcal{R} . A proof of any claim that this would be a good approximation of the true dynamics of the macroscopic variable x for a given example will have to invoke the following sequence of arguments. Initially assume that the microscopic system is a slow-fast system with a transversally stable slow manifold, for which the macroscopic quantity x is a coordinate. The first question is then: does the approximate coarse-level time stepper Φ converge to the true dynamics on the slow manifold in the limit $\varepsilon \rightarrow 0$, where ε is the parameter measuring the time scale separation? In addition to the case discussed here, equation-free analysis is also applied to high-dimensional, stochastic (or chaotic) systems showing macroscopic behavior because the dynamics of the microscopic degrees of freedom averages out rapidly [2, 38, 34]. In these cases another question must be addressed: in which sense is the averaging process approximating a classical slow-fast system?

1.1. An implicit coarse-level time stepper. Before equation-free analysis can be performed, one must find the restriction and lifting operators \mathcal{R} and \mathcal{L} . Fig-

ure 1.1 suggests the relation $\Phi(t; \cdot) = \mathcal{R} \circ \text{evolve} \circ \mathcal{L}$. However, this will not approximate the true macroscopic flow in general. Why? Let us assume that the microscopic system is slow-fast and the macroscopic system corresponds to the slow flow on the slow manifold in the coordinate x . Then an arbitrary choice of \mathcal{L} and \mathcal{R} does not lead to a coarse time-stepper Φ which approximates the slow flow in any way, even in the limit of infinite time scale separation ($\varepsilon \rightarrow 0$). The source of the error is an initialization of the microscopic system away from the slow manifold. One relies on the separation of time scales in a so-called healing step to reduce this error. However, in most reviews this healing is applied inconsistently [22, 23, 24]. That is, healing would not lead to Φ converging to the true slow flow in the limit of infinite time scale separation, even in the ideal case of a slow-fast system. A consistent way to perform healing are so-called *constrained-runs* corrections after lifting, developed in [12, 42, 43]. These papers developed schemes of increasing complexity to compensate for this error source.

An alternative, explained in Section 2, is to use an implicitly defined coarse-level time stepper Φ , where the slow flow is not measured at predetermined points in space but rather at healed points. In the special case of computation of equilibria, the use of the implicit time stepper reduces to the formula introduced as the “third method” by Vandekerckhove *et al* [39]. In Section 3, we give a detailed proof of the convergence of the implicitly defined coarse-level time stepper Φ to the flow on the slow manifold, answering the question of convergence for the implicit time stepper. The approximation error of Φ (under some transversality conditions) is exponentially small in the parameter ε measuring the time scale separation. Our theorem does not require that the time scale separation parameter ε approach zero, merely that it be sufficiently small. The precise statement is then that the error is of order $\exp(-Kt_{\text{skip}})$, where K is the rate of attraction transversal to the slow manifold and t_{skip} is the healing time. In Section 4 we discuss the assumptions and consequences of the convergence theorem and compare it to other results in the literature.

1.2. Macroscopic behavior of a microscopic traffic model. In Section 5 and Section 6 we apply the implicit coarse time stepper to a traffic modeling problem that fits into the framework of equation-free analysis: a large number of cars (the microscopic particles) on a circular road that interact with each other, resulting in so-called phantom jams moving slowly along the road against the direction of traffic, i.e., forming a traveling wave at the microscopic level.

The mathematical modeling and analysis of traffic flow dynamics has a considerable history (see, e.g., [17, 29, 31] for reviews). Macroscopic traffic models use partial differential equations, such as Burger’s equation [29], for modeling the flow. They model the density of cars as a continuous quantity to directly formulate macroscopic equations for density and flux along the road. In contrast, microscopic particle models (deterministic [1] or stochastic [19, 35]) can be used to describe the behavior of individual cars or drivers. An advantage of microscopic models is that parameters can be assigned directly to the individual drivers’ behavior (for example, aggressiveness, inertia, or reaction delay) such that these parameters’ influence and the trajectories of individual cars can be investigated. Another use of microscopic models is to test the effects of new devices for individual cars, for example, cruise control, on the overall traffic prior to their implementation in real traffic. In this paper we use the optimal velocity model [1] as an example of an underlying microscopic model. The optimal velocity model results in a set of coupled ordinary differential equations, but despite its simplicity it can reproduce the phenomenon of phantom traffic jams. An advantage of choosing the optimal velocity model is that we have guidance from the results

of direct bifurcation analysis of the full microscopic system when only a few cars are involved [11, 30] as well as from perturbation analysis based on the discrete modified Korteweg–de Vries equation [10]. Direct bifurcation analysis of the microscopic system becomes infeasible when the number of cars gets large. Furthermore, it is difficult to analyze macroscopic quantities for which typically no equations are explicitly given such as the mean and standard deviation of headways or densities of cars. In Section 6 we show how this difficulty can be tackled by using equation-free methods for the bifurcation analysis on a macroscopic level.

In Section 7 we summarize the obtained results and give an overview of open problems.

2. Nontechnical description of general equation-free analysis with implicit lifting. Equation-free analysis as described by [23] is motivated by ideas from the analysis of slow-fast systems: one assumes that on a long time scale the dynamics is determined by only a few state variables and the other state variables are *slaved*. Mathematically this means that the flow of a high-dimensional system under study converges rapidly onto a low-dimensional manifold on which the system is governed by an ordinary differential equation (ODE). In many practical applications convergence is achieved only in the sense of statistical mechanics (the effects of many particles averaging out; see [2, 6]). We give our description and subsequent convergence proofs of equation-free analysis using the terminology of slow-fast systems with transversally stable slow manifolds following the notation of [9]. The traffic problem discussed in Section 5 and 6 does not require the notion of weak (averaged) convergence.

2.1. The notion of a slow-fast system. Let

$$\dot{u} = f_\varepsilon(u) \tag{2.1}$$

be a smooth dynamical system defined for $u \in \mathbb{R}^D$, where f_ε depends smoothly on the parameter ε . We assume that ε is a *singular perturbation parameter*. This means that the flow M_ε generated by (2.1),

$$M_\varepsilon : \mathbb{R} \times \mathbb{R}^D \rightarrow \mathbb{R}^D, \quad (t; u) \mapsto M_\varepsilon(t; u)$$

has a whole smooth d -dimensional submanifold \mathcal{C}_0 of equilibria for $\varepsilon = 0$: if $u \in \mathcal{C}_0$, then $M_0(t; u) = u$ (and, thus, $f_0(u) = 0$) for all t . The dimension d is the number of slow variables. In the notation of singular perturbation theory, t measures the time on the *fast* time scale. We assume that this manifold \mathcal{C}_0 is transversally uniformly exponentially stable for $\varepsilon = 0$, which corresponds to the stable case of Fenichel’s geometric singular perturbation theory [9]. For this case we know that the flow $M_\varepsilon(t; \cdot)$ has a transversally stable invariant manifold \mathcal{C}_ε for small nonzero ε , too. This manifold \mathcal{C}_ε is called the slow manifold, and the flow M_ε , restricted to \mathcal{C}_ε , is called the slow flow. For the traffic problem the time scale separation is present as demonstrated numerically later in Section 5.2.

2.2. Lifting, restriction, and time stepping. The equation-free approach to coarse graining [23] does not require direct access to the right-hand side f_ε of the microscopic system (2.1) but merely the ability to evaluate $M_\varepsilon(t; u)$ for finite positive times t (typically $t \ll 1/\varepsilon$ in the fast time scale t) and arbitrary u . It also relies on two smooth maps that have to be chosen beforehand:

$$\begin{aligned} \mathcal{R} : \mathbb{R}^D &\rightarrow \mathbb{R}^d && \text{the restriction operator,} \\ \mathcal{L} : \mathbb{R}^d &\rightarrow \mathbb{R}^D && \text{the lifting operator.} \end{aligned}$$

In the optimal velocity model discussed in Section 6, \mathcal{R} is chosen as a mapping from headway profiles to the standard deviation σ and \mathcal{L} constructs a headway profile by using σ (cf. (6.3) and (6.4)).

The basic idea underlying [23] is that one can analyze the dynamics of (2.1) on the slow manifold \mathcal{C}_ε by studying a map in the space of restricted variables x in the domain of \mathcal{L} (called $\text{dom } \mathcal{L} \subset \mathbb{R}^d$) of the form (cf. Figure 1.1)

$$\text{Lift} \rightarrow \text{Evolve} \rightarrow \text{Restrict},$$

or, to be precise, the map

$$P_\varepsilon(t; \cdot) : x \mapsto \mathcal{R}(M_\varepsilon(t; \mathcal{L}(x))) = [\mathcal{R} \circ M_\varepsilon(t; \cdot) \circ \mathcal{L}](x) \quad (2.2)$$

for selected times $t \ll 1/\varepsilon$. The central question is: how can one compose a macroscopic time stepper, that is, an approximate time- δ map $\Phi(\delta, \cdot) : \mathbb{R}^d \rightarrow \mathbb{R}^d$, using coordinates in the domain of \mathcal{L} for the flow M_ε restricted to \mathcal{C}_ε ? One important observation is that this map Φ must be defined implicitly. Figure 2.1 shows how one can define a good approximate time- δ map $\Phi(\delta; \cdot)$. It contains an additional parameter t_{skip} , called the *healing time* in [23]. This healing time must be applied to both the argument x and the result y of Φ . Thus, $\Phi(\delta; \cdot)$ is given implicitly by solving

$$\begin{aligned} P_\varepsilon(t_{\text{skip}}; y) &= P_\varepsilon(t_{\text{skip}} + \delta; x), & \text{that is,} \\ \mathcal{R}(M_\varepsilon(t_{\text{skip}}; \mathcal{L}(y))) &= \mathcal{R}(M_\varepsilon(t_{\text{skip}} + \delta; \mathcal{L}(x))) \end{aligned} \quad (2.3)$$

for y , and setting $\Phi(\delta; x) := y$. Under some genericity conditions on \mathcal{R} , \mathcal{L} , and M_ε the order of approximation for Φ is exponentially accurate for increasing t_{skip} if we assume that $\varepsilon t_{\text{skip}}$ and $\varepsilon(t_{\text{skip}} + \delta)$ are bounded:

$$\|\Phi(\delta; x) - \Phi_*(\delta; x)\| \leq C \exp(-K t_{\text{skip}}). \quad (2.4)$$

In this estimate $K > 0$ and $C > 0$ are constants that depend only on a uniform upper bound T_{up} for $\varepsilon t_{\text{skip}}$ and $\varepsilon(t_{\text{skip}} + \delta)$. The flow Φ_* is the exact flow M_ε , restricted to the slow manifold \mathcal{C}_ε , in a suitable coordinate representation in $\text{dom } \mathcal{L}$. The same estimate holds also for the derivatives of Φ with respect to the initial value up to a fixed order (with more restrictive conditions on ε). So,

$$\|\partial_2^j \Phi(\delta; x) - \partial_2^j \Phi_*(\delta; x)\| \leq C \exp(-K t_{\text{skip}})$$

(possibly with other constants C) for derivative orders j less than a given k (the subscript of ∂_i^j refers to the argument of Φ with respect to which the j th derivative is taken). The degree of achievable differentiability is determined by the time scale separation: the smaller ε is, the smoother the slow manifold \mathcal{C}_ε is, and, thus, the higher we can choose the maximal derivative order k .

Based on the implicitly defined approximate flow map Φ , one can now perform higher-level tasks in equation-free analysis.

2.3. Bifurcation analysis of macroscopic equilibria. Bifurcation analysis for equilibria boils down to finding fixed points and their stability and bifurcations for $\Phi(\delta; \cdot)$ with some small, arbitrary δ (that is, $\delta \ll 1/\varepsilon$ in our notation). In terms of \mathcal{R} and \mathcal{L} , the equation $\Phi(\delta; x_0) = x_0$, defining the equilibrium x_0 , reads (cf. Figure 2.1)

$$\mathcal{R}(M_\varepsilon(t_{\text{skip}} + \delta; \mathcal{L}(x_0))) = \mathcal{R}(M_\varepsilon(t_{\text{skip}}; \mathcal{L}(x_0))). \quad (2.5)$$

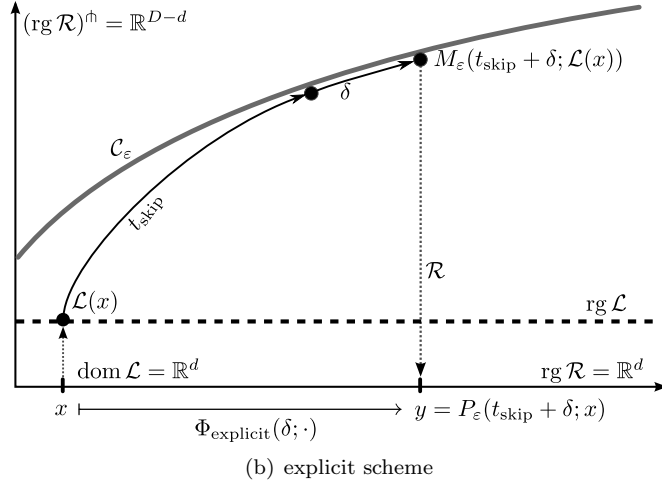
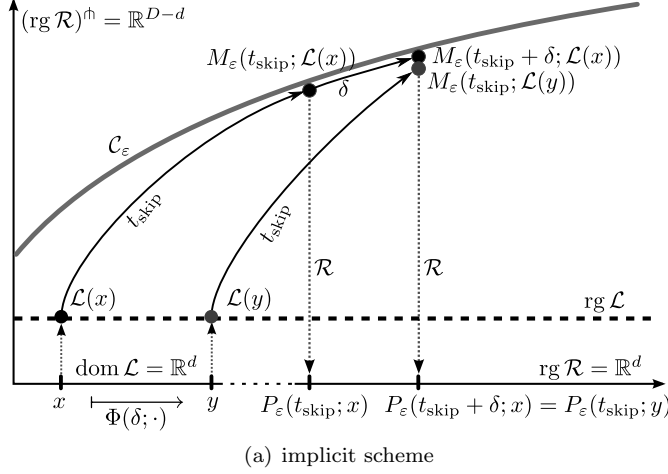


FIG. 2.1. (a) Sketch showing a typical geometry of the implicit scheme in a slow-fast system with a slow manifold C_ε and an arbitrary lifting \mathcal{L} and restriction \mathcal{R} . The healing $M_\varepsilon(t_{\text{skip}}; \cdot)$ is applied to all points in the domain of \mathcal{L} . Note that $\text{dom } \mathcal{L}$ and $\text{rg } \mathcal{R}$ can be different, but must have the same dimension. $(\text{rg } \mathcal{R})^\perp$ refers to an arbitrary transversal complement of $\text{rg } \mathcal{R}$. (b) The explicit scheme is shown for comparison.

This equation has been proposed and studied already in [39]. In applications, (2.5) is solved using a Newton iteration (cf. (6.9) in the optimal velocity model). Since the time stepper is defined implicitly, one finds the stability and bifurcations of an equilibrium x_0 by studying the generalized eigenvalue problem

$$\left[\frac{\partial}{\partial x} [\mathcal{R}(M_\varepsilon(t_{\text{skip}} + \delta; \mathcal{L}(x)))] \Big|_{x=x_0} \right] x = \lambda \left[\frac{\partial}{\partial x} [\mathcal{R}(M_\varepsilon(t_{\text{skip}}; \mathcal{L}(x)))] \Big|_{x=x_0} \right] x. \quad (2.6)$$

This eigenvalue problem will give the eigenvalues of the implicitly-known flow $\Phi(\delta; \cdot)$, linearized with respect to its second argument x in the equilibrium x_0 such that bifurcations occur when λ is on the unit circle.

2.4. Projective integration. In projective integration one approximates the ODE for the flow on the slow manifold C_ε in the coordinate $x \in \mathbb{R}^d$. The ODE for the

true flow Φ_* on the slow manifold is an implicit ODE with the solution $x(t)$, which will be derived in detail in Section 3. Its approximation based on Φ is

$$\frac{d}{dt} \mathcal{R}(M_\varepsilon(t_{\text{skip}}; \mathcal{L}(x))) = \frac{\partial}{\partial \delta} \mathcal{R}(M_\varepsilon(t_{\text{skip}} + \delta; \mathcal{L}(x))) \Big|_{\delta=0}. \quad (2.7)$$

For fixed t_{skip} the left-hand side is a function of $x \in \mathbb{R}^d$ such that the time-derivative of this function defines (implicitly) the time-derivative of x . The term inside the partial derivative on the right-hand side is a function of two arguments, δ and x , for which one takes the partial derivative with respect to its first argument δ in $\delta = 0$, making also the right-hand side a function of x only. Consequently, every integration scheme becomes implicit. For example, if one wants to perform an explicit Euler step of stepsize Δt starting from x_j at time t_j , this becomes an implicit scheme (defining x_{j+1} as the new value at time $t_{j+1} = t_j + \Delta t$):

$$\frac{1}{\Delta t} [P_\varepsilon(t_{\text{skip}}; x_{j+1}) - P_\varepsilon(t_{\text{skip}}; x_j)] = \frac{1}{\delta} [P_\varepsilon(t_{\text{skip}} + \delta; x_j) - P_\varepsilon(t_{\text{skip}}; x_j)], \quad (2.8)$$

or, in terms of restricting and lifting,

$$\begin{aligned} \mathcal{R}(M_\varepsilon(t_{\text{skip}}; \mathcal{L}(x_{j+1}))) - \mathcal{R}(M_\varepsilon(t_{\text{skip}}; \mathcal{L}(x_j))) \\ = \frac{\Delta t}{\delta} [\mathcal{R}(M_\varepsilon(t_{\text{skip}} + \delta; \mathcal{L}(x_j))) - \mathcal{R}(M_\varepsilon(t_{\text{skip}}; \mathcal{L}(x_j)))] \end{aligned}$$

Projective integration becomes attractive if either one can choose Δt much larger than t_{skip} and δ , or one can set Δt negative, enabling integration backward in time on the slow manifold (cf. (6.14) and Figure 6.1), even though the original system is very stiff in \mathbb{R}^D forward in time (and thus, strongly expanding backward in time). For positive Δt the restriction on the size of Δt is given by standard consistency and stability requirements of the coarse-grained integration method restricted to the slow flow (in general the restriction is $\varepsilon \Delta t \ll 1$, which makes the maximal stepsize independent of the time-scale separation). Note that during computation of residuals and Jacobian matrices one can evaluate $P_\varepsilon(t_{\text{skip}}; x)$ as a by-product of the evaluation of $P_\varepsilon(t_{\text{skip}} + \delta; x)$, assuming that the restriction \mathcal{R} is of comparatively low computational cost.

2.5. Matching the restriction. Sometimes it is of interest to find a microscopic state $u \in \mathbb{R}^D$ on the slow manifold \mathcal{C}_ε that has a particular $x \in \mathbb{R}^d$ as its restriction ($\mathcal{R}(u) = x$); see [12, 42, 43]. This state u is defined implicitly and can be found by solving the d -dimensional nonlinear equation

$$\mathcal{R}(M_\varepsilon(t_{\text{skip}}; \mathcal{L}(\tilde{x}))) = x \quad (2.9)$$

for \tilde{x} , and then setting $u = M_\varepsilon(t_{\text{skip}}; \mathcal{L}(\tilde{x}))$. This solution u is close to the true slow manifold \mathcal{C}_ε with an error of order $\exp(-K t_{\text{skip}})$, where the decay rate $K > 0$ and the possible constant in front of the exponential are independent of ε and t_{skip} . This implies that, if we choose $t_{\text{skip}} = O(\varepsilon^{-1})$ with $p \in (0, 1)$, the distance of u to \mathcal{C}_ε is small beyond all orders of ε (see Section 3 for the precise conditions). Equation (2.9) was also proposed and studied in [39] (called INITMAN in [39]), although without the general error estimate.

3. Convergence of equation-free analysis. This section gives a detailed discussion of the convergence results of the methods sketched in Section 2. Sections 5 and 6 study the optimal velocity model for traffic flow as an application of implicit equation-free analysis.

We formulate all assumptions on \mathcal{R} , \mathcal{L} , and M_ε for the singular perturbation parameter ε at $\varepsilon = 0$, even though it is typically difficult to vary ε in complex model simulations. However, stating the conditions at $\varepsilon = 0$ ensures that they are uniformly satisfied for all sufficiently small ε , which is the range of parameters for which the statements of this section are valid (cf. [9]). Throughout this section various constants will appear in front of exponentially growing or decaying quantities. As the concrete values of these constants do not play a role, we will use the same variable name C on all occasions without meaning them to be the same. We will state which quantities the constant C depends on whenever we use exponential estimates.

The notation ∂_k^j refers to the j th derivative with respect to the k th argument. For example, $\partial_2^j M_\varepsilon$ refers to the j th-order partial derivative of the flow M_ε with respect to its second argument (the starting point), and the zeroth derivative refers to the value of flow $M_\varepsilon(t; \cdot)$ itself.

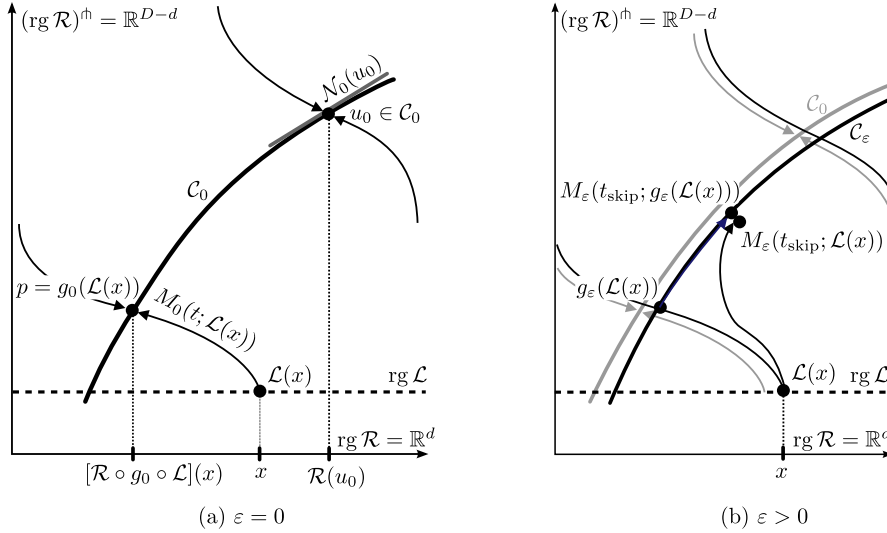


FIG. 3.1. Sketch of geometrical interpretation of transversality assumptions. Note that $(\text{rg } \mathcal{R})^h$ refers to an arbitrary transversal complement of $\text{rg } \mathcal{R}$. Panel (a) shows the geometry at $\varepsilon = 0$: The trajectory starting at $\mathcal{L}(x)$ must converge to \mathcal{C}_0 , and its limit is called $g_0(\mathcal{L}(x))$. The overall map $\mathcal{R} \circ g_0 \circ \mathcal{L}$ must be a local diffeomorphism. This entails that the Jacobian $\partial \mathcal{R}$ must have full rank on the tangent space $N_0(u_0)$ in any $u_0 \in \mathcal{C}_0$ (also shown in (a)), and that $\text{rg } \mathcal{L}$ intersects each fiber (the set of points u converging to the same $u_0 \in \mathcal{C}_0$) transversally. Shown in panel (b): g_ε and \mathcal{C}_ε are $O(\varepsilon)$ perturbations of g_0 and \mathcal{C}_0 , and $M_\varepsilon(t_{\text{skip}}; \mathcal{L}(x)) - M_\varepsilon(t_{\text{skip}}; g_\varepsilon(\mathcal{L}(x)))$ are $\exp(-Kt_{\text{skip}})$ close for $t_{\text{skip}} > 0$.

3.1. Existence of transversally stable slow manifold. As introduced in Section 2.1, the microscopic flow $M_\varepsilon(t; u_0)$ is the solution of

$$\dot{u} = f_\varepsilon(u), \quad u(t) \in \mathbb{R}^D, \quad (3.1)$$

starting from initial condition $u_0 \in \mathbb{R}^D$, which for $\varepsilon = 0$ has a d -dimensional manifold of equilibria \mathcal{C}_0 . That is, $f_0(u) = 0$ if $u \in \mathcal{C}_0$. In order to avoid the discussion of

what happens when the flow M_ε reaches certain boundaries or becomes large while following the slow dynamics, we assume that the manifold \mathcal{C}_0 of equilibria of M_0 is compact. Our first assumption guarantees transversal stability of \mathcal{C}_0 .

ASSUMPTION 1 (Separation of time scales and transversal stability). *There exists a constant $K_0 > 0$ such that for all points $u \in \mathcal{C}_0$ the Jacobian $\partial f_0(u)$ has $D-d$ eigenvalues with real part less than $-K_0$.*

This implies that the flow M_0 approaches the slow manifold \mathcal{C}_0 with a rate faster than K_0 from all initial conditions u in some neighborhood of \mathcal{C}_0 . That is, for every u in an appropriate open neighborhood \mathcal{U} of the slow manifold \mathcal{C}_0 there exists a point $p \in \mathcal{C}_0$ such that

$$\lim_{t \rightarrow \infty} M_0(t; u) = p$$

(note that for $\varepsilon = 0$ all points on the slow manifold \mathcal{C}_0 are equilibria), and the distance can be bounded via

$$\|M_0(t; u) - p\| \leq C \exp(-K_0 t) \|u - p\|, \quad \|\partial_2^j M_0(t; u)\| \leq C \exp(-K_0 t)$$

for all $t \geq 0$ and $j \geq 1$, where the constant C depends only on the derivative order j .

Since the slow manifold \mathcal{C}_0 is compact, one can choose a uniform constant C for all u in the neighborhood \mathcal{U} . The above assumption implies the existence of a smooth map (called the *stable fiber projection*),

$$g_0 : \mathcal{U} \rightarrow \mathcal{C}_0, \quad \text{defined by } g_0(u) := p, \quad (3.2)$$

assigning to each u its limit $p \in \mathcal{C}_0$ under the flow M_0 (see Figure 3.1(a)).

We recall now two central persistence results of classical singular perturbation theory [9]. First, the slow manifold \mathcal{C}_0 persists for sufficiently small ε , deforming to a smooth nearby manifold \mathcal{C}_ε (as shown in Figure 3.1(b)). This manifold \mathcal{C}_ε is also compact. Restricted to \mathcal{C}_ε , the flow M_ε is governed by a smooth ODE (the *slow flow*) with a right-hand side for which all derivatives up to a given order k are proportional to ε (larger k requires smaller ε):

$$\|f_\varepsilon(u)\| \leq \varepsilon, \quad \|\partial^j f_\varepsilon(u)[v_1, \dots, v_j]\| \leq \varepsilon \|v_1\| \cdots \|v_j\| \quad (3.3)$$

for all $j = \{1, \dots, k\}$, $u \in \mathcal{C}_\varepsilon$ and $v_1, \dots, v_j \in \mathcal{N}_\varepsilon(u)$. (Here $\mathcal{N}_\varepsilon(u)$ is the tangent space of \mathcal{C}_ε ; for $\varepsilon = 0$ it is the null space of the linearization of f_0 in u on the slow manifold \mathcal{C}_0 .) Note that typically one has only $\|\partial^j f_\varepsilon(u)|_{\mathcal{C}_\varepsilon}\| \leq C\varepsilon$, but we can set the constant C equal to unity without loss of generality by rescaling time or redefining the parameter ε . Thus, the flow $M_\varepsilon(t; \cdot)$ is a global diffeomorphism on the slow manifold \mathcal{C}_ε which has growth bounds of order ε forward and backward in time:

$$\|\partial_2^j M_\varepsilon(t; \cdot)|_{\mathcal{C}_\varepsilon}\| \leq C \exp(\varepsilon|t|), \quad \|\partial_2^j M_\varepsilon^{-1}(t; \cdot)|_{\mathcal{C}_\varepsilon}\| \leq C \exp(\varepsilon|t|), \quad (3.4)$$

for some constant C independent of t and ε and all derivative orders j up to a fixed order k . Note that $M_\varepsilon^{-1}(t; \cdot) = M_\varepsilon(-t; \cdot)$ exists for all times t as long as one restricts the flow M_ε to the slow manifold \mathcal{C}_ε .

Second, the stable fiber projection map g_0 persists for small ε , getting perturbed smoothly to a map g_ε , defined for each u in the neighborhood \mathcal{U} of the slow manifold \mathcal{C}_0 (and its perturbation \mathcal{C}_ε). The map g_ε picks for every point $u \in \mathcal{U}$ the unique point $g_\varepsilon(u)$ inside the slow manifold \mathcal{C}_ε such that the trajectories starting from u and $g_\varepsilon(u)$

converge to each other forward in time with an exponential rate K of order 1 (that is, K is uniformly positive for all sufficiently small ε and all $u \in \mathcal{U}$):

$$\|\partial_2^j M_\varepsilon(t; u) - \partial_2^j M_\varepsilon(t; g_\varepsilon(u))\| \leq C \exp(-Kt) \|u - g_\varepsilon(u)\| \quad (3.5)$$

for all $t \geq 0$, $u \in \mathcal{U}$, and $0 \leq j \leq k$, where the constant C is uniform for $u \in \mathcal{U}$. In general, the decay rate K has to be smaller than the rate K_0 asserted to exist in Assumption 1 for $\varepsilon = 0$. More precisely, for every rate $K < K_0$ there exists a range $(0, \varepsilon_0)$ of ε for which (3.5) holds. Choosing ε_0 smaller permits one to choose K closer to K_0 . The stable fiber projection map g_ε is an order- ε perturbation of g_0 :

$$\|\partial^j g_\varepsilon(u) - \partial^j g_0(u)\| \leq C\varepsilon \quad (3.6)$$

for all $j = \{0, \dots, k\}$ and a constant C that is uniform for all $u \in \mathcal{U}$. The black curves transversal to \mathcal{C}_ε in Figure 3.1(b) illustrate the fibers, that is, which points of \mathcal{U} get mapped onto the same point in \mathcal{C}_ε under g_ε . Note that the fibers are not trajectories for $\varepsilon > 0$; rather they are $(D - d)$ -dimensional manifolds.

3.2. Transversality conditions on restriction and lifting. One assumption on the restriction \mathcal{R} and the lifting \mathcal{L} is that they are both smooth maps.

Furthermore, we assume that the lifting operator \mathcal{L} maps some bounded open set $\text{dom } \mathcal{L} \subset \mathbb{R}^d$ into the basin of attraction \mathcal{U} of \mathcal{C}_0 for $\varepsilon = 0$. We will make all convergence statements in this section for $x \in \text{dom } \mathcal{L}$.

We formulate the transversality conditions on \mathcal{R} and \mathcal{L} with the help of the tangent space $\mathcal{N}_0(u)$ to the slow manifold \mathcal{C}_0 in a point $u_0 \in \mathcal{C}_0$, which is given as

$$\mathcal{N}_0(u_0) = \ker \partial f_0(u_0). \quad (3.7)$$

Remember that the stable fiber projection g_0 maps all $u \in \mathcal{U}$ onto the slow manifold \mathcal{C}_0 . The tangent space $\mathcal{N}_\varepsilon(u)$ to the perturbed slow manifold \mathcal{C}_ε in a point $u \in \mathcal{C}_\varepsilon$ is a perturbation of $\mathcal{N}_0(u)$ of order ε .

ASSUMPTION 2 (Transversality of \mathcal{R} and \mathcal{L}).

1. The map $g_0 \circ \mathcal{L}$ is a local diffeomorphism between $\text{dom } \mathcal{L} \subset \mathbb{R}^d$ and the slow manifold \mathcal{C}_0 for every $x \in \text{dom } \mathcal{L}$.
Equivalently, the composition of the linearizations $\partial g_0(\mathcal{L}(x)) \in \mathbb{R}^{D \times D}$ and $\partial \mathcal{L}(x) \in \mathbb{R}^{D \times d}$ has full rank for all $x \in \text{dom } \mathcal{L} \subset \mathbb{R}^d$.
2. The map $\mathcal{R} : \mathcal{U} \rightarrow \mathbb{R}^d$, restricted to the slow manifold \mathcal{C}_0 , is a local diffeomorphism between \mathcal{C}_0 and \mathbb{R}^d for every u in some relatively open subset $\text{dom } \mathcal{R} \cap \mathcal{C}_0$.
Equivalently, the dimension of the space $\partial \mathcal{R}(u) \mathcal{N}_0(u)$ equals d for every $u \in \text{dom } \mathcal{R} \cap \mathcal{C}_0$.
3. The set $\text{dom } \mathcal{R} \cap \mathcal{C}_0$ contains $g_0(\mathcal{L}(\text{dom } \mathcal{L}))$ as a subset, and the boundary of $\text{dom } \mathcal{R} \cap \mathcal{C}_0$ has a positive distance from the boundary of $g_0(\mathcal{L}(\text{dom } \mathcal{L}))$.

Note that points 1 and 2 of Assumption 2 are generically satisfied in a given $x \in \mathbb{R}^d$ or $u_0 \in \mathcal{C}_0$. By convention we keep $\text{dom } \mathcal{L}$ and $\text{dom } \mathcal{R}$ such that the transversality conditions are uniformly satisfied in $\text{dom } \mathcal{L}$ and $\text{dom } \mathcal{R}$. The assumption that $\text{dom } \mathcal{R}$ (the region where \mathcal{R} satisfies Assumption 2) contains the set $g_0(\mathcal{L}(\text{dom } \mathcal{L}))$ guarantees that the map $x \mapsto \mathcal{R}(g_0(\mathcal{L}(x)))$ is locally invertible for all $x \in \text{dom } \mathcal{L}$ and that its linearization is uniformly regular in $\text{dom } \mathcal{L}$. All points of Assumption 2 and the invertibility of the slow flow, $M_\varepsilon(t; \cdot)$ restricted to the slow manifold \mathcal{C}_ε , can be combined to ensure that the map

$$\mathbb{R}^d \supseteq \text{dom } \mathcal{L} \ni x \mapsto \mathcal{R}(M_\varepsilon(t; g_\varepsilon(\mathcal{L}(x)))) \in \mathbb{R}^d \quad (3.8)$$

is locally invertible for all $\varepsilon \in [0, \varepsilon_0)$ and for all times t satisfying

$$|t| \leq T_{\text{up}}/\varepsilon \quad (3.9)$$

for some constant T_{up} . The constant T_{up} is independent of ε , t , and $x \in \text{dom } \mathcal{L}$. It is determined by the distance between the boundaries of $\text{dom } \mathcal{R}$ and $g_\varepsilon(\mathcal{L}(\text{dom } \mathcal{L}))$. This distance is positive because of point 3 in Assumption 2 and the fact that g_ε is a small perturbation of g_0 . Then the time it takes a trajectory on \mathcal{C}_ε to reach the boundary of $\text{dom } \mathcal{R}$ starting from $g_\varepsilon(\mathcal{L}(\text{dom } \mathcal{L}))$ is of order $1/\varepsilon$ such that we can introduce the constant T_{up} . All components of the map (3.8) are locally invertible: $g_\varepsilon \circ \mathcal{L} : \text{dom } \mathcal{L} \rightarrow \mathcal{C}_\varepsilon$ by Point 1 of Assumption 2 (transversality of \mathcal{L}); $M_\varepsilon(t; \cdot)$ is a diffeomorphism on \mathcal{C}_ε ; and \mathcal{R} , restricted to \mathcal{C}_0 (and, hence, to \mathcal{C}_ε), is also locally invertible due to Point 2 of Assumption 2. For $\varepsilon = 0$ the map (3.8) is independent of t . Moreover, the norm of the derivative of the map (3.8) and its inverse are also uniformly bounded if $|\varepsilon t| \leq T_{\text{up}}$.

3.3. Map of exact flow M_ε into \mathbb{R}^d . Next, we give a coordinate system and a constructive procedure that maps the flow M_ε , restricted to the slow manifold \mathcal{C}_ε , back to \mathbb{R}^d . This kind of map is called a “lifting” of the flow M_ε on \mathcal{C}_ε to its cover \mathbb{R}^d in, e.g., [9], but we do not use this term here to avoid confusion with the lifting operation \mathcal{L} , used in an equation-free context (cf. for example [23]). For any fixed t_{skip} the following map $X_\varepsilon : \text{dom } \mathcal{L} \rightarrow \mathcal{C}_\varepsilon$ introduces coordinates of (part of) \mathcal{C}_ε in $\text{dom } \mathcal{L}$:

$$X_\varepsilon(x) = M_\varepsilon(t_{\text{skip}}; g_\varepsilon(\mathcal{L}(x))).$$

This map is locally invertible because $g_0 \circ \mathcal{L}$ is a local diffeomorphism between $\text{dom } \mathcal{L}$ and \mathcal{C}_0 (and, hence, $g_\varepsilon \circ \mathcal{L}$ is a diffeomorphism between $\text{dom } \mathcal{L}$ and \mathcal{C}_ε for small ε), and $M_\varepsilon(t_{\text{skip}}; \cdot)$ is a global diffeomorphism on \mathcal{C}_ε (see (3.4)). Moreover, if $M_\varepsilon(t_{\text{skip}}; g_\varepsilon(\mathcal{L}(x)))$ is in the interior of the domain of \mathcal{R} , then one can find, for a given $u = X_\varepsilon(x) \in \mathcal{C}_\varepsilon$, a preimage $\tilde{x} \approx x$ of any point $\tilde{u} \in \mathcal{C}_\varepsilon$ close to u by solving

$$\mathcal{R}(X_\varepsilon(\tilde{x})) = \mathcal{R}(\tilde{u}) \quad (3.10)$$

for \tilde{x} . This follows from Assumption 2 (transversality for \mathcal{R}). In particular, point 3 of Assumption 2 gives the bound on the range of t_{skip} for which the linearization of (3.10) is regular: the trajectory $t \mapsto M_\varepsilon(t; g_\varepsilon(\mathcal{L}(x)))$ should not leave $\text{dom } \mathcal{R}$ for $t \in [0, t_{\text{skip}}]$, which is guaranteed for $t_{\text{skip}} < T_{\text{up}}/\varepsilon$. By requiring $\tilde{x} \approx x$, the preimage \tilde{x} of \tilde{u} , defined by (3.10), becomes unique.

Let $x(\delta) \in \text{dom } \mathcal{L} \subset \mathbb{R}^d$ be a trajectory of the flow M_ε on \mathcal{C}_ε in the coordinates defined by X_ε . By definition, x satisfies $X_\varepsilon(x(\delta)) = M_\varepsilon(\delta; X_\varepsilon(x(0)))$. As long as $X_\varepsilon(x(\delta))$ is in the domain of \mathcal{R} , we can apply \mathcal{R} to this identity to obtain

$$\begin{aligned} \mathcal{R}(X_\varepsilon(x(\delta))) &= \mathcal{R}(M_\varepsilon(\delta; X_\varepsilon(x(0))), & \text{that is,} \\ \mathcal{R}(M_\varepsilon(t_{\text{skip}}; g_\varepsilon(\mathcal{L}(x(\delta)))) &= \mathcal{R}(M_\varepsilon(t_{\text{skip}} + \delta; g_\varepsilon(\mathcal{L}(x(0)))) \end{aligned} \quad (3.11)$$

(inserting the definition of X_ε). Hence, the flow M_ε on \mathcal{C}_ε , written in the coordinates $x \in \text{dom } \mathcal{L}$, satisfies the implicit ODE

$$\frac{d}{dt} \mathcal{R}(M_\varepsilon(t_{\text{skip}}; g_\varepsilon(\mathcal{L}(x)))) = \frac{\partial}{\partial \delta} \mathcal{R}(M_\varepsilon(t_{\text{skip}} + \delta; g_\varepsilon(\mathcal{L}(x)))) \Big|_{\delta=0} \quad (3.12)$$

as long as $\varepsilon t_{\text{skip}} < T_{\text{up}}$ and $\varepsilon(t_{\text{skip}} + \delta) < T_{\text{up}}$ such that the resulting trajectory $x(\delta)$ stays in $\text{dom } \mathcal{L}$ and $X_\varepsilon(x(\delta)) = M_\varepsilon(t_{\text{skip}}; g_\varepsilon(\mathcal{L}(x(\delta))))$ stays in $\text{dom } \mathcal{R}$. For different

values of t_{skip} we get different coordinate representations of the same flow, all related to the representation with $t_{\text{skip}} = 0$ via the global diffeomorphism $M_\varepsilon(t_{\text{skip}}; \cdot)$ on \mathcal{C}_ε , which is a near-identity transformation if $t_{\text{skip}} \ll 1/\varepsilon$ (see (3.4)).

Let us denote the flow corresponding to the trajectory $x(\delta)$ in (3.11) as $\Phi_*(\delta; \cdot) : \text{dom } \mathcal{L} \rightarrow \text{dom } \mathcal{L}$. The flow Φ_* is generated by the ODE (3.12). If $\varepsilon t_{\text{skip}} \leq T_{\text{up}}$ and $\delta \ll 1/\varepsilon$, this flow map $\Phi_*(\delta; \cdot)$ is defined implicitly by solving the following system for y_* ,

$$\mathcal{R}(M_\varepsilon(t_{\text{skip}}; g_\varepsilon(\mathcal{L}(y_*)))) = \mathcal{R}(M_\varepsilon(t_{\text{skip}} + \delta; g_\varepsilon(\mathcal{L}(x))))), \quad (3.13)$$

and setting $\Phi_*(\delta; x) := y_*$. The local invertibility of X_ε guarantees that there is a solution y_* close to x and that the solution y_* is unique in the vicinity of x . For larger δ , one breaks down the flow into smaller time steps such that one can apply the local solvability at every step:

$$\Phi_*(\delta; x) = \Phi_*(\delta/m; \cdot)^m[x] \quad (3.14)$$

for sufficiently large integer m . This construction of Φ_* achieves a representation of the exact flow M_ε restricted to \mathcal{C}_ε that is globally unique on $\text{dom } \mathcal{L}$ for all δ with $\varepsilon(t_{\text{skip}} + \delta) \leq T_{\text{up}}$.

3.4. Approximate flow map and its convergence. We now define the approximate flow map $y = \Phi(\delta; x)$. Its definition is similar to (3.13), in particular, it is also implicit. To highlight where the difference between y and y_* comes from, we put the defining equation for $y_* = \Phi_*(\delta; x)$ directly below the implicit definition of y :

$$\begin{aligned} \mathcal{R}(M_\varepsilon(t_{\text{skip}}; \mathcal{L}(y))) &= \mathcal{R}(M_\varepsilon(t_{\text{skip}} + \delta; \mathcal{L}(x))), \\ \mathcal{R}(M_\varepsilon(t_{\text{skip}}; g_\varepsilon(\mathcal{L}(y_*)))) &= \mathcal{R}(M_\varepsilon(t_{\text{skip}} + \delta; g_\varepsilon(\mathcal{L}(x)))), \end{aligned} \quad (3.15)$$

where the equation at the top defines $y = \Phi(\delta; x)$. To check how the difference $y - y_*$ depends on x , t_{skip} , δ , and ε we use a regular perturbation argument by comparing solutions of the two equations in (3.15). We rely on (3.5), which guarantees that the perturbations are small, and the invertibility of the map (3.8), which guarantees that the linearization of the left-hand side with respect to y and its inverse are uniformly bounded for $\varepsilon(t_{\text{skip}} + \delta) \leq T_{\text{up}}$.

THEOREM 3.1 (Convergence of approximate flow map). *Let $K \in (0, K_0)$ be a given constant. We assume that the assumptions on time scale separation (Assumption 1) and transversality (Assumption 2) hold for \mathcal{L} , M_ε and \mathcal{R} such that*

$$x \mapsto \mathcal{R}(M_\varepsilon(t; g_\varepsilon(\mathcal{L}(x))))$$

is a local diffeomorphism if $|\varepsilon t| \leq T_{\text{up}}$ with some $T_{\text{up}} > 0$ that is uniform for all ε and all $x \in \text{dom } \mathcal{L}$.

Then there exist a lower bound t_0 for t_{skip} , an upper bound ε_0 for ε , and a constant $C > 0$ such that $y = \Phi(\delta; x)$ and $y_ = \Phi_*(\delta; x)$ are well defined by (3.15), and the estimate*

$$\|\partial_2^j \Phi(\delta; x) - \partial_2^j \Phi_*(\delta; x)\| \leq C \exp(-K t_{\text{skip}}) \quad (3.16)$$

holds for all orders $j \in \{0, \dots, k\}$, all $x \in \text{dom } \mathcal{L}$, $\varepsilon \in (0, \varepsilon_0)$, $t_{\text{skip}} \in (t_0, T_{\text{up}}/\varepsilon]$, and $\delta \in [0, T_{\text{up}}/\varepsilon - t_{\text{skip}}]$.

(Remember that k is defined above (3.3).) Note that the assumptions of Theorem 3.1 require that $\varepsilon t_{\text{skip}}$ and $\varepsilon(t_{\text{skip}} + \delta)$ be bounded by T_{up} . Hence, the theorem

ensures convergence of $\Phi(\delta; x)$ to $\Phi_*(\delta; x)$ only if $t_{\text{skip}} \rightarrow \infty$ and $\varepsilon \rightarrow 0$ simultaneously. Since ε is usually fixed in applications, this theorem is not enough to ensure convergence for $t_{\text{skip}} \rightarrow \infty$ uniform for ε .

The proof of Theorem 3.1 splits the error $\Phi(\delta; x) - \Phi_*(\delta; x)$ using the fiber projection g_ε . The projection of the error onto \mathcal{C}_ε using g_ε is zero by construction, and the error transversal to the manifold decays exponentially due to (3.5), giving a perturbation of order $\exp(-Kt_{\text{skip}})$. This implies that we can apply the implicit function theorem if $\varepsilon(t_{\text{skip}} + \delta) \leq T_{\text{up}}$, giving an error of order $\exp(-Kt_{\text{skip}})$ for the difference $y - y_*$ and for the first- and higher-order derivatives. The details of the proof are given in Appendix A.

4. Discussion of the general convergence statement and its assumptions. Theorem 3.1 is a local statement with respect to x , claiming convergence only in a region $\text{dom } \mathcal{L}$ in which the transversality conditions are uniformly satisfied. One has to restrict the times t_{skip} and δ such that the slow flow $M_\varepsilon(t; g_\varepsilon(x))$ cannot leave the region $g_\varepsilon(\text{dom } \mathcal{R})$ for the times $t = t_{\text{skip}}$ and $t = t_{\text{skip}} + \delta$. This is appropriate because in many cases, during continuation or projective integration the maps \mathcal{R} and \mathcal{L} get adapted (for example, for the traffic problem investigated in Section 6, \mathcal{L} is varied along the curve of macroscopic equilibria).

4.1. Comparison to the explicit equation-free approach. The convergence theorem, Theorem 3.1, implies that for smaller ε and a longer healing time t_{skip} the deviation from the true flow reduces as long as $\varepsilon(t_{\text{skip}} + \delta) \leq T_{\text{up}}$ and $\varepsilon t_{\text{skip}} \leq T_{\text{up}}$. This is in contrast to the approach proposed by [23], where the coarse flow map was defined in an explicit way: $\Phi_{\text{explicit}}(\delta; x) = \mathcal{R}(M_\varepsilon(\delta; \mathcal{L}(x)))$ or $\Phi_{\text{explicit}}(\delta; x) = \mathcal{R}(M_\varepsilon(\delta + t_{\text{skip}}; \mathcal{L}(x)))$ [28, 37, 5]. Following this approach, one would analyze equilibria of the slow flow and their stability by studying fixed points of the map

$$\Phi_{\text{explicit}}(t; \cdot) : x \mapsto \mathcal{R}(M_\varepsilon(t; \mathcal{L}(x))) \quad (4.1)$$

for x , where $0 < t \ll 1/\varepsilon$ is chosen such that it includes a healing time t_{skip} ($t > t_{\text{skip}}$). (Compare (4.1) with definition (3.15): $y = \Phi(\delta; x)$ if $\mathcal{R}(M_\varepsilon(t_{\text{skip}}; \mathcal{L}(y))) = \mathcal{R}(M_\varepsilon(t_{\text{skip}} + \delta; \mathcal{L}(x)))$.) For $1 \ll t \ll 1/\varepsilon$ the map $\Phi_{\text{explicit}}(t; \cdot)$ is a perturbation of order $O(\varepsilon t) \ll 1$ of the map $x \mapsto \mathcal{R}(g_0(\mathcal{L}(x)))$. Any flow map on the slow manifold must be a perturbation of the identity of order εt for small εt . Thus, the explicit map $\Phi_{\text{explicit}}(t; \cdot)$ can be a valid approximation for the flow on the slow manifold in any coordinates only if $\mathcal{R} \circ g_0 \circ \mathcal{L}$ equals the identity on \mathbb{R}^d . Often this requirement is approximated by $\mathcal{R} \circ \mathcal{L} = I$, because g_0 is in general unknown [21, 26, 27, 33, 36]. Note that there is no ε - or t dependence in the limiting map $\mathcal{R} \circ g_0 \circ \mathcal{L}$, resulting in the much more restrictive condition $\mathcal{R} \circ g_0 \circ \mathcal{L} = I$ than transversality Assumption 2 on \mathcal{R} and \mathcal{L} . Moreover, $\mathcal{R} \circ g_0 \circ \mathcal{L} = I$ is only a consistency condition, making it possible for $\Phi_{\text{explicit}}(t; \cdot)$ to resemble the map of a slow flow. If this consistency condition is violated, then $\Phi_{\text{explicit}}(t; \cdot)$ will show dynamics independent of the properties of the flow on the slow manifold. For example, if the map $\mathcal{R} \circ g_0 \circ \mathcal{L}$ has a stable fixed point, then $\Phi_{\text{explicit}}(t; \cdot)$ will also have a stable fixed point independent of the slow flow M_ε on \mathcal{C}_ε .

One way to ensure that the operator Φ_{explicit} approximates the slow flow is to construct a lifting operator that maps onto the slow manifold \mathcal{C}_ε . This has been achieved up to finite order of ε through constrained-runs corrections to \mathcal{L} [42, 43]. In our notation the first-order version of this scheme would correspond to defining the lifting $\mathcal{L} : \mathbb{R}^d \ni x \mapsto u \in \mathbb{R}^D$ as the (locally unique) u satisfying $\mathcal{R}(u) = x$

and $d/dt(\mathcal{R}^\dagger(u)) = 0$ (zero-derivative principle), where \mathcal{R}^\dagger is an arbitrary operator satisfying $\mathbb{R}^D = \ker \mathcal{R} \oplus \ker \mathcal{R}^\dagger$. Zagaris *et al.* [42, 43] developed general m th-order versions of this scheme. Vandekerckhove *et al.* [39] compared the constrained-runs schemes from [42, 43] to the results of the implicit expression (2.9) (called INITMAN in [39]) for various examples, finding (2.9) uniformly vastly superior in terms of convergence and performance. Equation (2.9) also requires only the solution of a d -dimensional, not a D -dimensional, system (usually $d \ll D$). Using (3.11) it is not necessary to find a microscopic state u on the slow manifold matching a particular restriction x ($\mathcal{R}u = x$). A usage of INITMAN prefixed at each single step of an explicit equation-free scheme would do so and is an alternative. Recognizing that the slow flow is given by an implicit ODE from the beginning reduces the computational overhead, because matching the restriction is required only at user-specified points.

4.2. Testing the transversality conditions and choosing the healing time and coarse dimension. The conditions listed in Assumption 1 and Assumption 2 contain terms that are unknown in practice. For example, the fiber projection g_0 and the tangent space \mathcal{N}_0 to the slow manifold are both inaccessible because in many cases one cannot vary the time scale separation parameter ε . However, observing the minimal singular value of the linearization $\partial_2 P_\varepsilon(t_{\text{skip}}; x) = \partial/\partial x[\mathcal{R}(M_\varepsilon(t_{\text{skip}}; \mathcal{L}(x)))]$ with respect to x (a d -dimensional matrix) provides an indicator: in points where the transversality condition is violated, the linearization becomes singular.

Similarly, the condition number of the linearization $\partial_2 P_\varepsilon(t_{\text{skip}}; x)$, $\text{cond } \partial_2 P_\varepsilon(t_{\text{skip}}; x)$, guides the choice of the optimal healing time t_{skip} . All tasks involve solving nonlinear equations with a Jacobian $\partial_2 P_\varepsilon(t_{\text{skip}}; x)$. While the error due to finite time scale separation becomes smaller, $\text{cond } \partial_2 P_\varepsilon(t_{\text{skip}}; x)$ can grow with t_{skip} such that other errors may become dominant when they are amplified by $\text{cond } \partial_2 P_\varepsilon(t_{\text{skip}}; x)$. In particular, when the microscopic system is a Monte Carlo simulation, a trajectory $M_\varepsilon(t; u)$ is determined via ensemble runs, and the accuracy of the evaluation of M_ε is only of the order of $1/\sqrt{S}$, where S is the ensemble size.

The linearization $\partial_2 P_\varepsilon(t_{\text{skip}}; x)$ also helps to reveal whether one has too many coarse variables, that is, whether d is too large such that the flow M_ε restricted to the assumed slow manifold \mathcal{C}_ε is not sufficiently slow (still containing rapidly decaying components). Then $\partial_2 P_\varepsilon(t_{\text{skip}}; x)$ becomes close to singular, too. Note that any solution found, for example, by solving the fixed point equation (2.5) is still a correctly identified fixed point with correctly identified stability. However, the linearization of (2.5) becomes close to singular.

4.3. Chaotic and stochastic systems. Barkley, Kevrekidis, and Stuart [2] analyzed how the equation-free approach can be used to analyze moment maps of stochastic systems or high-dimensional chaotic systems that converge in a statistical mechanics sense to low-dimensional stochastic differential equations (SDEs). These moment maps play then the same role as the macroscopic map $\Phi(\delta; \cdot)$ in our case. The authors of [2] observe that the choice of δ strongly influences the number and stability of fixed points. Also the inclusion of additional macroscopic variables (increasing d) changes the results of the equation-free analysis qualitatively. It is unclear how the implicit scheme (2.3) behaves in the situations studied by [2]. While [2] also invokes a separation-of-time-scales argument to study approximation quality for the stochastic systems, their setting does not fit into the assumptions underlying Fenichel's theorem but requires weaker notions of convergence based on averaging over a chaotic attractor (see [13] for a review). An adaptation of the analysis in [2], and possibly further adaptation of the implicit scheme (2.3), is the missing link between Theorem 3.1 es-

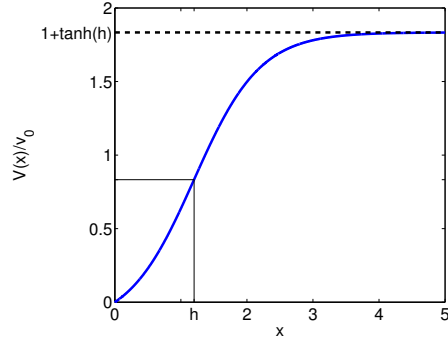


FIG. 5.1. Optimal velocity function $V(x)/v_0$ defined in (5.4) for $h = 1.2$. The maximal velocity $v_0(1 + \tanh(h))$ is obtained for $x \rightarrow \infty$. v_0 acts as a scaling parameter for V . The inflection point of the optimal velocity function V is at h .

tabulating convergence for the idealized situation, given in Section 3, and applications of equation-free analysis to stochastic or chaotic systems.

5. Traffic Modeling — The Optimal Velocity Model. We now turn to the equation-free analysis of a system that fits into the framework of implicit equation-free analysis. We will perform some of the typical tasks listed in Section 2 and apply the implicit equation-free analysis introduced in Sections 2 and 3.

We consider N cars driving around a ring road of length L . The individual drivers' behavior is assumed to be uniform and deterministic, modeled by an optimal velocity model [1] of the form

$$\tau \ddot{x}_n + \dot{x}_n = V(x_{n+1} - x_n), \quad n = 1, 2, \dots, N \quad (5.1)$$

where x_n is the position of car n , τ is the inertia of the driver and car, and V is an optimal velocity function, prescribing the preferred speed of the driver depending on the distance to the car in front (the *headway*). The ring road implies periodic boundary conditions in space

$$x_{n+N} = x_n + L. \quad (5.2)$$

In order to do numerical bifurcation analysis, we rewrite the second-order ODE (5.1) as a system of first-order ODEs:

$$\begin{aligned} \dot{x}_n &= y_n \\ \dot{y}_n &= \tau^{-1} [V(x_{n+1} - x_n) - y_n]. \end{aligned} \quad (5.3)$$

Similar to [1, 10] we choose the function

$$V(\Delta x_n) = v_0(\tanh(\Delta x_n - h) + \tanh(h)), \quad (5.4)$$

shown in Figure 5.1, as the optimal velocity function. In (5.4), $v_0(1 + \tanh(h))$ is the maximal velocity, $\Delta x_n := x_{n+1} - x_n$ is the headway, and the inflection point h of V determines the desired safety distance between cars. The reviews [17, 29, 31] put behavioral models based on optimal velocity functions into the general context of traffic modeling and discuss possible choices of optimal velocity functions. One conclusion from [31] is that the choice of V does not affect the overall bifurcation

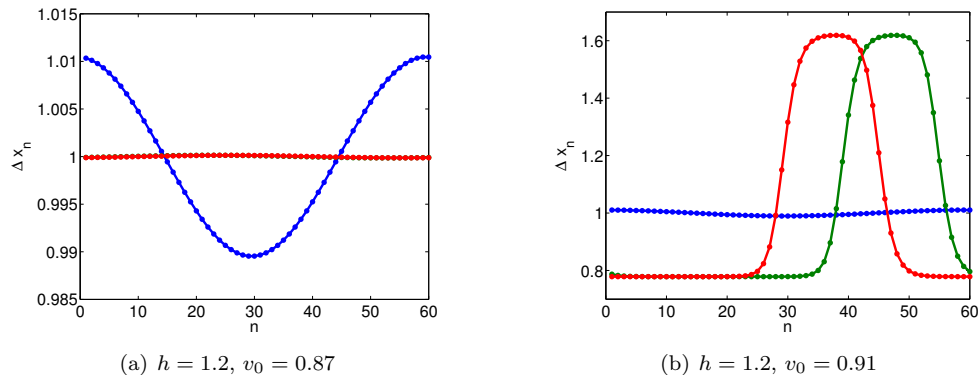


FIG. 5.2. Comparison of the two traffic flow regimes. The initial condition (blue) is compared with the final state (red = $T = 5 \times 10^4$, green = $T - 500$). (a) Free flow regime. (b) Traffic jam regime. Note the different scales of Δx_n on the vertical axis.

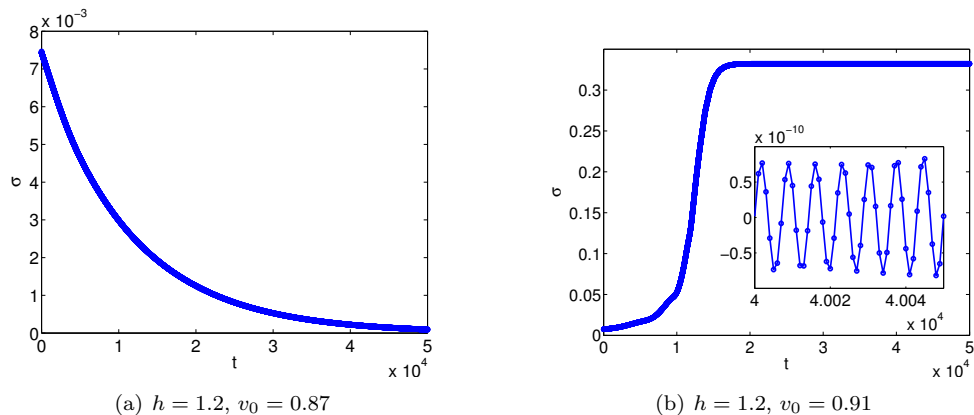


FIG. 5.3. Time evolution of the macroscopic variable σ for the same parameters as in Figure 5.2. (a) The decay to the stable free flow. (b) Using the same initial condition as in (a), the system converges to a stable traffic jam. The inset in (b) shows the difference between the macroscopic variable σ and its long-term average σ^* over the last 10000 time steps of the simulation. One expects small oscillations of σ in time due to the finite number of cars. However, these small oscillations are below the tolerance of the ODE solver.

diagram of a single jam qualitatively (some choices of V can give rise to unphysical behavior such as cars briefly moving backwards, though). Depending on parameters and initial conditions, the system either shows free-flow behavior, that is, all cars move with the same velocity and headway, or it develops traffic jams, which means that there coexist regions of uniformly small headways and low speeds, spatially alternating with regions of free flow with uniformly large headways and large speeds. We focus on the dynamics near the formation of a single jam. In equilibrium the single traffic jam moves along the ring with nearly (due to a finite number of cars) constant shape and speed as a traveling wave against the direction of traffic. In the full system (5.3) the single traffic jam is a traveling wave perturbed by small periodic oscillations; see Figure 5.3(b) below.

5.1. Direct Simulations. The uniform flow, starting from initial condition

$$\begin{aligned} x_n(0) &= (n-1) \frac{L}{N} \\ y_n(0) &= V \left(\frac{L}{N} \right), \end{aligned} \tag{5.5}$$

is a solution of (5.3), where all cars move with the same velocity $y_n(t) = V(\frac{L}{N})$ and headway $\Delta x_n(t) = \frac{L}{N}$. We focus on two types of long-time behavior, the uniform flow and traveling wave solutions. To give a qualitative picture of these, we run two simulations, initializing system (5.3) with initial conditions close to the uniform flow, or adding a periodic perturbation of strength μ :

$$\begin{aligned} x_n(0) &= (n-1) \frac{L}{N} + \mu \sin \left(\frac{2\pi}{N} n \right) \\ y_n(0) &= V \left(\frac{L}{N} \right). \end{aligned} \tag{5.6}$$

For all simulations, we use $N = L = 60$. The simulations were run for a time $T = 5 \cdot 10^4$ using the MATLAB `ode45`-solver [18] with absolute and relative tolerance 10^{-8} . All parameters for the simulation can be found in table B.1 in Appendix B. For our one-parameter analysis, we also fix the desired safety distance $h = 1.2$. Figures 5.2 and 5.3 show the long-time behavior of the initial condition (5.6) for the velocity parameters $v_0 = 0.87$ and $v_0 = 0.91$, respectively. In Figure 5.2, the headway is shown as a function of car number. It can be seen that the initial perturbation decays to the uniform flow for the trajectory for $v_0 = 0.87$ but converges to a traveling wave solution for $v_0 = 0.91$.

We choose the standard deviation σ for the headway as the macroscopic measure (called x in sections 2 and 3) describing the traffic flow

$$\sigma = \sqrt{\frac{1}{N-1} \sum_{n=1}^N (\Delta x_n - \langle \Delta x \rangle)^2}, \quad \text{where } \Delta x_n = x_{n+1} - x_n. \tag{5.7}$$

Here, $\langle \Delta x \rangle = 1$ is the mean of all headways. The free flow corresponds to $\sigma = 0$ and the decay of σ to the free flow is shown in Figure 5.3(a). If v_0 is chosen equal to 0.91, σ increases until it settles to an equilibrium, where a traveling wave of fixed shape is observed. It can be seen in the inset of Figure 5.3(b) that the macroscopic variable oscillates even in its steady state. These small-scale oscillations are expected due to the finite number of cars, because cars arrive at the rear and leave from the front of the jam at periodic intervals. However, the oscillation amplitude is orders of magnitude smaller than the macroscopic dynamics, such that the oscillations are obscured by discretization effects of the ODE solver (which shows subtolerance oscillations even for systems with stable equilibria).

5.2. Time scale separation. In order to apply the theoretical results from Sections 2 and 3, we have to check the extent to which the assumption about separation of time scales is valid. Initially, we use simulations to estimate the time scale separation, showing that the studied one-jam solution forms a one-dimensional stable submanifold, which we will then study in Section 6.

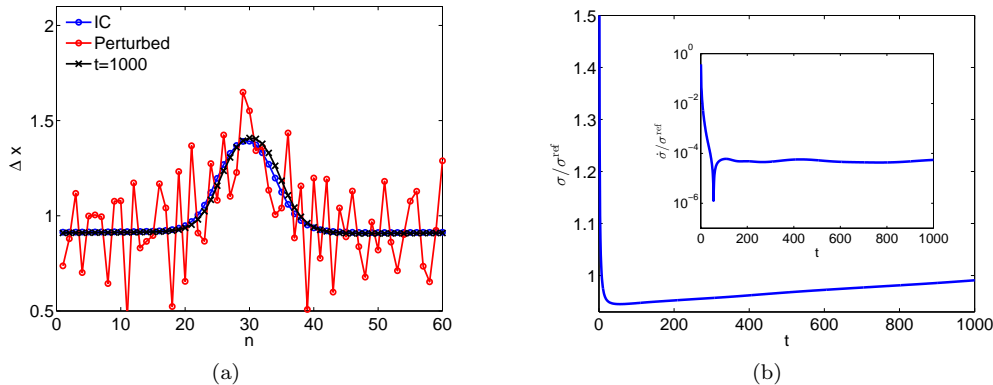


FIG. 5.4. Visualization of the time scale separation for system (5.3). (a) An initial nonequilibrium traffic jam (blue circles) is perturbed with uniformly distributed noise to yield a new profile (red circles). A microscopic simulation of 1000 time steps brings the system back to a single traffic jam (black crosses), which is slightly more pronounced than the initial jam. (b) The same simulation as in (a) shown in the macroscopic variable σ (scaled with $\sigma^{\text{ref}} = 0.16$). After a short time ($t \approx 10$), the system relaxes to a one-jam solution. During this process, σ is decreased drastically and settles on the fast time scale (see inset). Afterwards, σ increases again on a four-orders-of-magnitude slower time scale.

The simulation result shown in Figure 5.4 highlights that a one-dimensional slow manifold exists corresponding to a single jam. For Figure 5.4 we perturbed an initial nonequilibrium traffic jam (blue circles) by adding random numbers drawn from a uniform distribution in $[-0.5, 0.5]$. This perturbed state (red circles) is then simulated using (5.3) for 1000 time steps. The resulting state is observed to rapidly converge back to a single-jam solution (black crosses). Note that the drift of the jams has been subtracted in order to center the profiles for a better comparison. In Figure 5.4(a) the traffic jam at time $t = 1000$ is very slightly more pronounced than the initial jam (which was in nonequilibrium position, though). The time scale separation can be observed clearly in the time evolution of the macroscopic variable σ (cf. Figure 5.4(b)). For a very short time ($t \approx 10$), the macroscopic variable adjusts rapidly. This corresponds to the fast scale (see inset in Figure 5.4(b)). Observing the system for a much longer time of $t = 1000$, the slow drift in the macroscopic variable corresponds to the slow time scale. A numerical inspection yields a time-scale separation of approximately four orders of magnitude, i.e., $\varepsilon \approx 10^{-4}$, which appears to be different from $1/N$ (cf. also Figure 5.3 for visualizations of the slow dynamics).

The next section presents an equation-free bifurcation analysis for jam formation on the macroscopic level.

6. Equation-Free Bifurcation Analysis. We choose a one-dimensional macroscopic description; that is, the standard deviation σ is the only macroscopic variable. The change of the chosen macroscopic variable σ is studied with respect to system parameters. According to the equation-free approach presented in Section 2 the macroscopic ODE has the implicit form

$$\frac{d}{dt}\mathcal{R}(M(t_{\text{skip}}, \mathcal{L}(\sigma))) = \frac{\partial}{\partial \delta}\mathcal{R}(M(t_{\text{skip}} + \delta, \mathcal{L}(\sigma)))\Big|_{\delta=0}, \quad (6.1)$$

where the derivative on the right-hand side is approximated by the finite-difference quotient with finite δ

$$F(\sigma) = \frac{\mathcal{R}M(t_{\text{skip}} + \delta, \mathcal{L}(\sigma)) - \mathcal{R}M(t_{\text{skip}}, \mathcal{L}(\sigma))}{\delta}, \quad (6.2)$$

and t_{skip} is the healing time, which should be chosen long enough for transients to decay (cf. the discussion in Section 5.2).

As explained in Section 2 and 3, the equation-free setup avoids an analytical derivation of a macroscopic ODE but uses (6.1) where (6.2) is evaluated by simulation bursts of length $t_{\text{skip}} + \delta$. A good choice for the time δ depends on the slow dynamics. We used numerical observations to obtain a good estimate for (6.2), see also Figure 5.4. Note that the left- and right-hand sides in (6.1) depend also on the system parameters h and v_0 , which are not expressly included in (6.1) and (6.2). We also drop the subscript ε of M because it enters our system only indirectly. In order to find trajectories or equilibria of (6.1)–(6.2), it is necessary to define a lifting operator \mathcal{L} and a restriction operator \mathcal{R} . In our case, the restriction operator \mathcal{R} is given by the definition of the macroscopic measure in (5.7), i.e.,

$$\mathcal{R}(u) = \sqrt{\frac{1}{N-1} \sum_{n=1}^N (\Delta x_n - \langle \Delta x \rangle)^2}. \quad (6.3)$$

Our lifting operator constructs initial conditions with the help of a reference state $\tilde{u} = (\tilde{x}, \tilde{y}) \in \mathbb{R}^{2N}$, obtained during a previous microscopic simulation. We have to guarantee that the lifting \mathcal{L} initializes the system into the vicinity of the solution of interest, which we described in Section 3 as \mathcal{L} having to map into the attracting neighborhood \mathcal{U} of the slow manifold.

The following description assumes that microscopic simulations start and end near a single-pulse traffic jam. The components of the reference state \tilde{u} are the positions $(\tilde{x}_n)_{n=1}^N$ and the velocities $(\tilde{y}_n)_{n=1}^N$ of the cars (cf. (5.3)). Let us denote the macroscopic state corresponding to \tilde{u} by $\tilde{\sigma} = \mathcal{R}(\tilde{u})$. Given a real parameter p , whose meaning we shall explain in detail below, and a reference state \tilde{u} , we define $\mathcal{L}_{p, \tilde{u}}(\sigma)$ to be

$$\begin{aligned} \mathcal{L}_{p, \tilde{u}}(\sigma) = u = (x, y) &= (x_{\text{new}}, y_{\text{new}}) \in \mathbb{R}^N \times \mathbb{R}^N, & \text{where} \\ \Delta x_{\text{new}} &= \frac{p\sigma}{\tilde{\sigma}} \left(\Delta \tilde{x} - \langle \Delta \tilde{x} \rangle \right) + \langle \Delta \tilde{x} \rangle, \\ x_{\text{new}, 1} &= 0, & x_{\text{new}, n} = \sum_{i=1}^{n-1} \Delta x_{\text{new}, i} & \quad n = 2, \dots, N, \\ y_{\text{new}, n} &= V(\Delta x_{\text{new}, n}) & \quad n = 1, \dots, N. \end{aligned} \quad (6.4)$$

V is the optimal velocity function (5.4), $\langle \cdot \rangle$ refers to the average of a quantity, and $\Delta \tilde{x}$ are the headways of the reference state ($\Delta \tilde{x}_n = \tilde{x}_{n+1} - \tilde{x}_n$). In (6.4) we compute the positions $x \in \mathbb{R}^N$ first and then initialize the velocities $y \in \mathbb{R}^N$ by using the optimal velocity function for these positions. The positions are initialized such that $x_1 = 0$, resulting in a unique mapping from headways to positions. The definition (6.4) of $\mathcal{L}_{p, \tilde{u}}$ contains an artificial parameter p , which we keep equal to unity throughout, except for Figure 6.2 in Section 6.1 and the error estimates in Section 6.2. A parameter value of $p \neq 1$ introduces a systematic bias into our lifting such that we can vary p

gradually to investigate how our results depend on our choice of lifting. For $p \neq 1$, the lifting $\mathcal{L}_{p,\bar{u}}$ violates the common assumption of equation-free computations, where the identity $\mathcal{R} \circ \mathcal{L} = I$ is claimed to be necessary [33, 26, 21, 27, 36]. An application of $\mathcal{L}_{p,\bar{u}}$ and \mathcal{R} without any time evolution in between, yields $\mathcal{R}(\mathcal{L}_{p,\bar{u}}(\sigma)) = p \cdot \sigma$.

In the following, we use an equation-free pseudoarclength continuation scheme to compute bifurcation diagrams for the fixed point of (6.1)–(6.2); that is, we track a root curve (branch) of

$$F(\sigma, v_0) = 0 \tag{6.5}$$

in the (σ, v_0) -plane for the macroscopic right-hand side (6.2). The influence of speed limits on traffic jam formation motivates the choice of the velocity parameter v_0 as a bifurcation parameter. In (6.5) we include the bifurcation parameter v_0 explicitly as an argument of F . The pseudoarclength continuation contains two steps. The first step is a predictor step, where we use a secant predictor, assuming that we know two points on the branch already. Let (σ^0, v_0^0) and (σ^1, v_0^1) be those two points. We define the secant direction by

$$w = (\sigma^1 - \sigma^0, v_0^1 - v_0^0). \tag{6.6}$$

The prediction $(\hat{\sigma}, \hat{v}_0)$ for the next point on the branch is then determined by the secant predictor

$$(\hat{\sigma}, \hat{v}_0) = (\sigma^1, v_0^1) + s \frac{w}{\|w\|}, \tag{6.7}$$

where we keep the stepsize of the predictor uniformly at $s = 10^{-3}$. The prediction is not exactly on the branch and must be corrected in the following corrector step, which is chosen to be perpendicular to the predictor direction (6.6). The corrector step solves the system

$$\begin{aligned} F(\sigma, v_0) &= 0 \\ w^{(\sigma)}(\sigma - \hat{\sigma}) + w^{(v_0)}(v_0 - \hat{v}_0) &= 0, \end{aligned} \tag{6.8}$$

where $w^{(\sigma)}$ and $w^{(v_0)}$ are the components of w in the σ and v_0 direction, respectively. System (6.8) can be solved with respect to σ and v_0 by Newton's method using

$$(\sigma^{k+1}, v_0^{k+1})^T = (\sigma^k, v_0^k) + \nu J^{-1} F(\sigma^k, v_0^k), \tag{6.9}$$

where J is the Jacobian of the left-hand side of (6.8), given by

$$J = \begin{pmatrix} F_\sigma & F_{v_0} \\ w^{(\sigma)} & w^{(v_0)} \end{pmatrix}, \tag{6.10}$$

and ν is a relaxation parameter adjusting the length of a Newton step. For all computations we used a full Newton step, that is, $\nu = 1$. If the information on the Jacobian of the system is poor, for example, in noisy or stochastic systems, it might be useful to use a damped Newton method ($\nu < 1$). The iteration is initialized with the predictor (6.7)

$$(\sigma^0, v_0^0) = (\hat{\sigma}, \hat{v}_0). \tag{6.11}$$

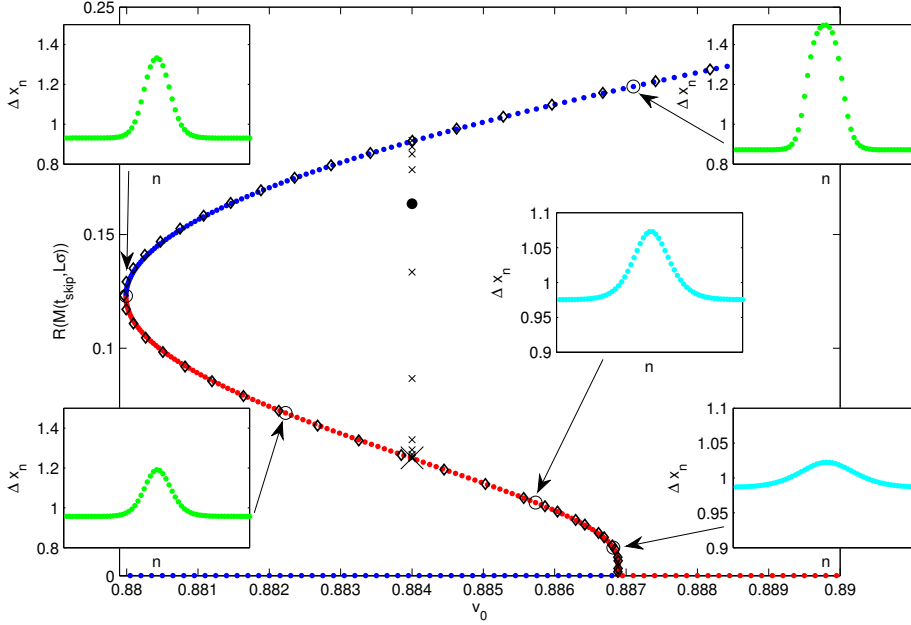


FIG. 6.1. Bifurcation diagram obtained by equation-free pseudoarclength continuation for $h = 1.2$. The traffic jam profiles are shown for selected points in the bifurcation diagram, marked with black circles. Note the change in scale on the vertical axes on the profiles for better visibility (horizontal axes show the car number n , vertical axes show headways). A fold point has been detected at $(v_0, \mathcal{R}(M(t_{\text{skip}}, \mathcal{L}\sigma))) \approx (0.88, 0.125)$, where a change in stability is observed. The blue dots mark stable states, while the red dots mark unstable states. It is due to the equation-free continuation that unstable branches can be observed. For the lifting we use (5.6) and (6.4) for continuation of the uniform flow and the traveling wave solution, respectively. Additionally, the black crosses mark a backward trajectory computed by using (6.14). Starting from the stable branch, the backward integration converges to the unstable branch (big cross). The black dot is the base point used for an error estimate in Figure 6.4. Black diamonds denote the results of a direct continuation of the full microscopic system on the macroscopic level. The data is in perfect agreement with results from implicit equation-free methods.

During the iteration the function F has to be evaluated according to its definition (6.2). This means that we lift, run the simulation of the microscopic system and then restrict with $t_{\text{skip}} = 300$ and $\delta = 2000$.

The Jacobian J is approximated via finite differences. Since $w^{(\sigma)}$ and $w^{(v_0)}$ are known from the predictor step, we only have to determine F_σ and F_{v_0} . We evaluated F at the points

$$(\sigma, v_0), \quad (\sigma + \Delta\sigma, v_0), \quad (\sigma, v_0 + \Delta v_0) \quad (6.12)$$

and computed the one-sided derivatives

$$F_\sigma = \frac{F(\sigma + \Delta\sigma, v_0) - F(\sigma, v_0)}{\Delta\sigma}, \quad F_{v_0} = \frac{F(\sigma, v_0 + \Delta v_0) - F(\sigma, v_0)}{\Delta v_0}. \quad (6.13)$$

We started the one-parameter continuation of the traffic jam in the direction of decreasing v_0 from two profiles obtained by direct simulations at $v_0 = 0.91$ and $v_0 = 0.9$. The resulting bifurcation diagram is shown in Figure 6.1.

The traffic jam, i.e., traveling wave, is stable for large values of v_0 . When following the branch, a saddle-node bifurcation is detected at $(\mathcal{R}(M(t_{\text{skip}}, \mathcal{L}\sigma))^*, v_0^*) \approx$

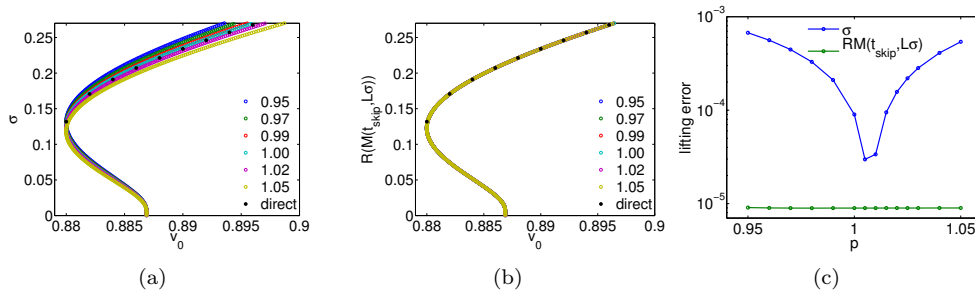


FIG. 6.2. (a) Bifurcation diagram obtained from running the implicit equation-free continuation scheme described in Section 6 for $p = 0.95, 0.97, 0.99, 1.0, 1.02, 1.05$. The black dots show the results from a direct downsweep of the stable branch. Depending on the value of p , the results differ visibly from the direct simulation data, which is usually used as an argument for finding a ‘good’ lifting operator. (b) The healed version of the bifurcation diagram; i.e., $\sigma^{\text{healed}} = \mathcal{RM}(t_{\text{skip}}, \mathcal{L}_p, \bar{u}\sigma)$ for different p all collapse to the same curve, fitting the direct numerical results perfectly. See also the main text in Section 2. (c) Analysis of the lifting error. The blue data points show the distances between the equation-free solution $v_0(\sigma)$ and the restriction of the simulation data using eq. (6.16) as a measure for the error. The results from a direct simulation of the stable branch are used as a reference curve (cf. Figure 6.2(a)). For the ‘normal’ equation-free data, i.e., using the unhealed macroscopic quantities, it is observed that the error is minimal at $p = 1.005$, corresponding to a ‘good’ lifting operator. The green data points show the behavior of the healed version of the bifurcation branches (cf. Figure 6.2(b)). The error is uniformly small when using the healed data. $h = 1.2$ for all images.

(0.88, 0.125), where the traffic jam changes stability. A further decrease of v_0 at that point would make the traffic jam dissolve. But due to the equation-free pseudoarclength continuation of the continuous branch, it is possible to follow the branch around the fold point and continue the unstable branch for increasing v_0 . The traffic jam stays unstable until it reaches the uniform flow at $\sigma = 0$ at a Hopf bifurcation point (cf. Section 6.3 and (6.24)). The microscopic states corresponding to selected points along the branch are shown as insets in Figure 6.1. The shape has sharp layers and a flat plateau on the stable branch, and becomes harmonic close to the equilibrium value $\sigma = 0$. Additionally, the time steps of a backward integration are shown for $v_0 = 0.884$, showing the heteroclinic connection between stable and unstable jams. The trajectory starts for $t_0 = 0$ at the stable branch. The Euler scheme (2.8) is used for computing the backward trajectory; that is,

$$\mathcal{RM}(t_{\text{skip}}, \mathcal{L}(\sigma_{j+1})) = \mathcal{RM}(t_{\text{skip}}, \mathcal{L}(\sigma_j)) + F(\sigma_j)\Delta t, \quad (6.14)$$

where σ_j is the solution at $t_j = j\Delta t$, and $\Delta t = -5000$ is chosen. The size of Δt is determined by the desired accuracy of the coarse projective integration. For the computation of $F(\sigma)$ the parameters from Table B.1 in Appendix B are chosen in (6.2). The backward integration converges to the unstable branch.

6.1. The influence of the choice of lifting operator. Figure 6.2 shows how the results depend on the artificial parameter p , which we introduced into the lifting operator $\mathcal{L}_{p, \bar{u}}$. In both panels, the same bifurcation diagram is shown for several values of p and compared to the restrictions of the stable fixed points of direct long-time simulations ($T = 3 \cdot 10^5$, black dots). The case where the usual equation-free identity $\mathcal{R} \circ \mathcal{L}_{p, \bar{u}} = I$ is fulfilled corresponds to $p = 1$. We observe that the preimages σ of the equilibria under the combination of lifting operator and healing $M(t_{\text{skip}}; \mathcal{L}_{p, \bar{u}}(\cdot))$

depend visibly on p (panel (a) of Figure 6.2). Therefore, we compare Figure 6.2(a) with the corresponding Figure 6.2(b) for the healed macroscopic quantity

$$\sigma_{\text{healed}} = \mathcal{R}(M(t_{\text{skip}}, \mathcal{L}_{p, \bar{u}} \sigma)) \quad (6.15)$$

for each macroscopic equilibrium σ along the branch of the bifurcation diagram. According to Section 3 the map $\mathcal{R}(M(t_{\text{skip}}, \mathcal{L}_{p, \bar{u}} \sigma))$ is a local diffeomorphism from \mathbb{R}^d into \mathbb{R}^d with $d = 1$. Plotting the bifurcation diagram in the $(v_0, \sigma_{\text{healed}})$ -plane in Figure 6.2(b), we obtain a solution branch that is independent of the choice of the lifting operator, as one would expect from Theorem 3.1.

For a more detailed analysis of the error, we compute the \mathbb{L}_2 norm between the interpolated data sets $v_0(\sigma)$ (expressing the parameter as a function of the equilibrium location near the fold) for the direct simulation data and the data for the stable branch of the equation-free bifurcation diagram. For interpolation, the MATLAB `interp1` function [18] with the “`spline`” option is used. We use the error measure

$$\|f - g\|^2 = \int_a^b [f(\sigma) - g(\sigma)]^2 d\sigma \quad (6.16)$$

to analyze the deviation between the restriction of the direct simulation data and equation-free continuation data. Here, f and g are the interpolated data sets $v_0(\sigma)$ for the simulated data and the equation-free data, respectively, in the range of σ between $a = 0.125$ and $b = 0.25$. The unstable branches cannot be compared with direct integration of the system. The deviation E using eq. (6.16) with lifting parameter p is shown in Figure 6.2(c). The blue data points correspond to the distance between the restriction of the simulation data and the equation-free solutions (that is, the preimages of the equation-free microscopic solutions under $M(t_{\text{skip}}; \mathcal{L}_{p, \bar{u}}(\cdot))$ in the domain of $\mathcal{L}_{p, \bar{u}}$). The distance is small for values of p close to 1, where the usual identity $\mathcal{R} \circ \mathcal{L} = I$ is fulfilled. However, the distance for σ_{healed} (green data) is uniformly small, independent of the choice of p . Therefore, healed quantities should be used when comparing equation-free results to restrictions of the direct simulation data. The uniformly small errors in Figure 6.2(c) (in green) suggest that with implicit time steppers the results are not sensitive to the choice of the lifting operator. This is in contrast to most equation-free applications [23, 5, 21], which use explicit time steppers of the form $\Phi(\delta; x) = \mathcal{R}(M(\delta; \mathcal{L}(x)))$.

6.2. Influence of the healing time t_{skip} and comparison to explicit scheme.

In this section, we investigate the influence of t_{skip} on the equation-free results, e.g., bifurcation diagrams and stability analysis. First, we show that the bifurcation diagrams are rather insensitive to the choice of t_{skip} , while the information of the Jacobian depends more noticeably on the value of t_{skip} .

The bifurcation diagrams obtained for $h = 1.2$ and $t_{\text{skip}} = 10, 100, 300, 1000, 2000$ are shown in Figure 6.3. In Figure 6.3(a) it can be observed that the bifurcation diagrams are similar for all choices of t_{skip} ; i.e., they show the same qualitative features. Although the bifurcation diagrams are quantitatively close to each other, the information about the derivatives, i.e., the Jacobian $\partial F / \partial \sigma$, does not appear to converge to a particular value for increasing t_{skip} . Note that the scale of the y -axis is 10^{-4} in this region of the bifurcation diagram, which suggests that the slow time scale is of this order.

For all values of t_{skip} , the fold point near $\sigma = 0.12$ is detected by a sign change in the Jacobian (cf. Figure 6.3(b)). Close to the Hopf point (which would appear

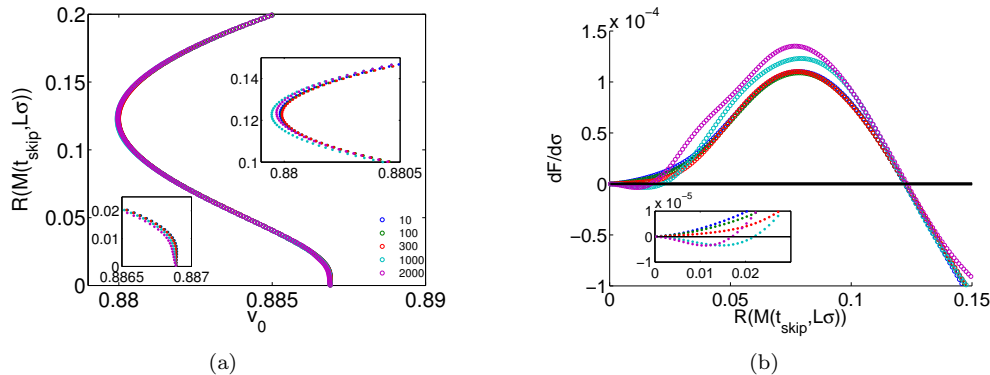


FIG. 6.3. (a) Bifurcation diagrams for $h = 1.2$ and $t_{\text{skip}} = 10, 100, 300, 1000, 2000$ in the healed quantities of σ . The difference between the curves is very small. Insets show a zoom for the fold and the Hopf point. (b) Comparison of the Jacobians for the different values of t_{skip} along the curve. Close to the Hopf point the value of the Jacobian does not converge for increasing t_{skip} within the plotted range.

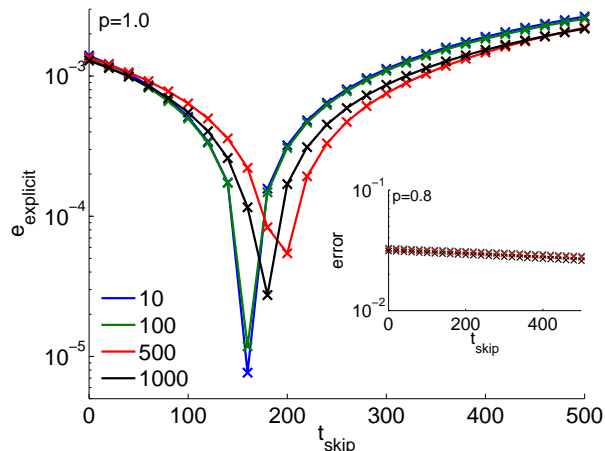


FIG. 6.4. Error analysis for the healing time t_{skip} in the explicit scheme, showing the error $e_{\text{explicit}} = |\Phi_{\text{explicit}} - \Phi_*|$ defined in (6.17). Colors indicate different values for δ . The inset shows the same computation for a scaled lifting operator $\mathcal{L}_{p, \bar{u}}$ with $p = 0.8$. Here, the explicit method has an error which is about two orders of magnitude larger than that for a good lifting operator $p = 1.0$. Note that explicit equation-free computations usually require $\mathcal{R} \circ \mathcal{L} = I$, and the choice of $p = 0.8$ violates this assumption.

as a pitchfork bifurcation in the macroscopic system (6.1)) the derivative $\partial F/\partial \sigma$ is not sufficiently accurate to resolve the criticality of the Hopf (pitchfork) bifurcation, which appears to be close to being degenerate. The Hopf bifurcation point cannot be studied using the operator \mathcal{R} because expression (6.3), defining \mathcal{R} , is singular in the uniform flow.

To study the influence of t_{skip} on the explicit scheme Φ_{explicit} and the implicit scheme Φ in more detail, we compare the results generated by the approximate macroscopic flow directly to a pregenerated trajectory of the microscopic flow. To this end we perform a long-term microscopic simulation of the traffic model from a reference point (Figure 6.1, black dot). After a sufficiently long transient, the dynamics settle

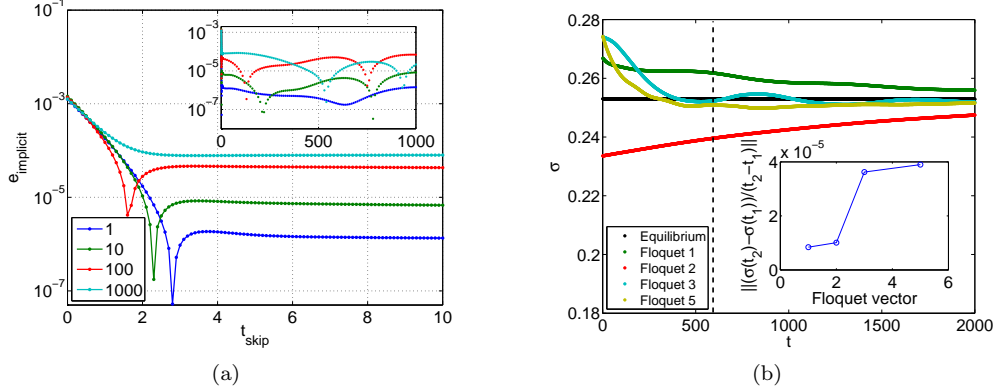


FIG. 6.5. (a) Dependence of the error e_{implicit} given by (6.18). The error is shown in dependence on t_{skip} for $\delta = 1, 10, 100, 1000$ (see color code in the legend); $h = 1.2, v_0 = 0.884, p = 0.8$. (b) Evolution of the system for perturbations in the directions of the leading Floquet vectors (cf. also Figure 6.6 for leading Floquet exponents). These perturbations lead to oscillations in the macroscopic description. The inset shows the decay rate over a time $t_2 - t_1 = 600$. While the perturbations in the first two Floquet eigenvectors decay with almost the same rate, there is a gap to the next Floquet vector number 3.

to the slow manifold. We denote the point at the end of this transient as $u(0) = \tilde{u}$. The microscopic trajectory $u(t)$ starting from \tilde{u} is always close to the slow manifold. The macroscopic state corresponding to \tilde{u} is denoted by $\tilde{\sigma} = \mathcal{R}(\tilde{u})$. The error of the explicit equation-free approach (scheme (4.1)) is then

$$\begin{aligned} e_{\text{explicit}}(t_{\text{skip}}, \delta; \mathcal{R}(\tilde{u})) &= |\Phi_{\text{explicit}}(\delta; \mathcal{R}(\tilde{u})) - \mathcal{R}(u(\delta))| \\ &= |\mathcal{R}(M(t_{\text{skip}} + \delta; \mathcal{L}_{p, \tilde{u}} \mathcal{R}(\tilde{u}))) - \mathcal{R}u(\delta)|. \end{aligned} \quad (6.17)$$

Figure 6.4 shows this error for several fixed δ and varying t_{skip} .

The error e_{explicit} is of order 10^{-3} to 10^{-5} for a good lifting operator, i.e., $p = 1.0$. The downward peak around $t_{\text{skip}} \approx 150$ in Figure 6.4 in logarithmic scale corresponds to a sign change of the scalar quantity $\mathcal{R}(M(t_{\text{skip}} + \delta; \mathcal{L}_{p, \tilde{u}} \mathcal{R}(\tilde{u}))) - \mathcal{R}u(\delta)$ in (6.17). For this healing time $t_{\text{skip}} \approx 150$ the lifted state is mapped into the stable fiber corresponding to \tilde{u} ; that is, $\tilde{u} = g_\varepsilon(M(t_{\text{skip}}; \mathcal{L}_{p, \tilde{u}}(\mathcal{R}(\tilde{u}))))$. Note that for a one-dimensional slow manifold the stable fibers are codimension-one surfaces (called isochrones if the slow manifold is a periodic orbit) such that we can expect to find the fiber for which the error goes to zero for $\delta \rightarrow \infty$ by varying the healing time t_{skip} . However, this appropriate healing time may depend on the point \tilde{u} on the slow manifold and is in general not known. The inset in Figure 6.4 shows the error e_{explicit} for a nonoptimal lifting operator $\mathcal{L}_{p, \tilde{u}}$, namely for $p = 0.8$. The error for the explicit method is of order 10^{-1} to 10^{-2} uniformly for t_{skip} and δ . Hence, for the explicit scheme varying t_{skip} can in general not compensate for errors introduced by the lifting operator.

When estimating the error e_{implicit} of the implicit scheme we have to first find the point σ corresponding to $\tilde{\sigma}$ after healing. Hence, the error e_{implicit} is given as

$$\begin{aligned} e_{\text{implicit}}(t_{\text{skip}}, \delta; \mathcal{R}(\tilde{u})) &= |\mathcal{R}(M(t_{\text{skip}} + \delta; \mathcal{L}_{p, \tilde{u}}(\sigma))) - \mathcal{R}(u(\delta))| \quad \text{where } \sigma \text{ solves} \\ &\mathcal{R}(\tilde{u}) = \mathcal{R}(M(t_{\text{skip}}; \mathcal{L}_{p, \tilde{u}}(\sigma))). \end{aligned} \quad (6.18)$$

Figure 6.5(a) shows e_{implicit} for $p = 0.8$ (such that the lifting operator is expected to be at some distance from the slow manifold initially), the same fixed integration times

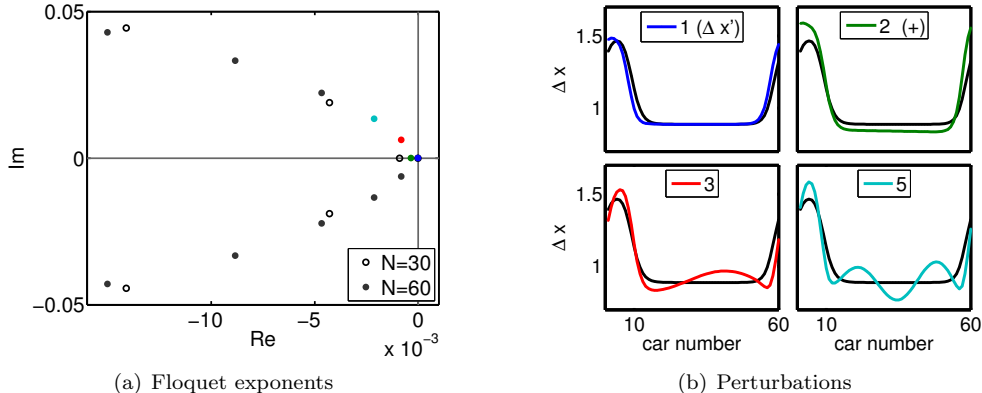


FIG. 6.6. Floquet exponents (a) and leading Floquet vectors (b) of a single traffic jam (viewed as a periodic orbit of the full system (5.3)). The orbit (shown in (b)) is also highlighted in Figure 6.1 ($v_0 = 0.884$ on stable branch). In (a), we have included the spectrum of a comparable orbit for $N = 30$, $L = 30$. In (b) we have added the Floquet vectors for the dominant Floquet exponents as a perturbation to the periodic orbit. Vectors 3 and 5 are complex. (+): Vector 2 has been orthonormalized with respect to vector 1.

δ as in Figure 6.4, and a range of t_{skip} from 0 to 1000 (see inset in Figure 6.5(a)).

After an initial decay over a few orders of magnitude (see Figure 6.5(a) main graph) the error starts to oscillate (see inset in Figure 6.5(a)) on a small scale compared to the value of the macroscopic variable. These small-scale oscillations suggest that the assumptions of Theorem 3.1 on large time scale separation are not satisfied for the traffic flow M . To confirm this we compute the Floquet exponents for the stable stationary single-traffic-jam solution (diamond at $v_0 = 0.884$ at the end of the heteroclinic connection marked by crosses in Figure 6.1). This is a periodic orbit of the microscopic system (5.3). Figure 6.6(a) shows the leading Floquet exponents for this periodic orbit. It shows a dominant real Floquet exponent very close to the origin next to the trivial Floquet exponent 0 (which corresponds to the flow direction). This dominant real Floquet exponent corresponds to the slow time scale that the equation-free analysis attempts to capture.

Figure 6.6(a) also shows that this dominant Floquet exponent is part of a band of complex Floquet exponents that is parabola-shaped and bending toward the half-plane with negative real part (see, for example, the band of full dots in Figure 6.6(a)). The spectra for the two system sizes plotted in Figure 6.6(a) indicate that the spacing of the Floquet exponents' frequency decreases with increasing N . The parabolic shape of the band then gives a gradually increasing spectral gap for the low-frequency Floquet exponents until finite-size effects become visible (to the right of the part of the complex plane shown in Figure 6.6(a)). The spectral gap between the dominant and the following Floquet exponents gives an upper bound on the time scale separation that is much more restrictive than the initial assessment in Figure 5.4 suggested.

An explanation for the apparent discrepancy is the mode shape of the eigenvectors corresponding to the low-frequency (slow-decay) Floquet exponents shown in Figure 6.6(b). Figure 6.6(b) illustrates how perturbations into the directions of the eigenvectors for the first five Floquet exponents look (ordered by descending real parts of the exponent). The first Floquet vector corresponds to the time derivative (the linearization of the time shift). The second Floquet vector corresponds to the dominant

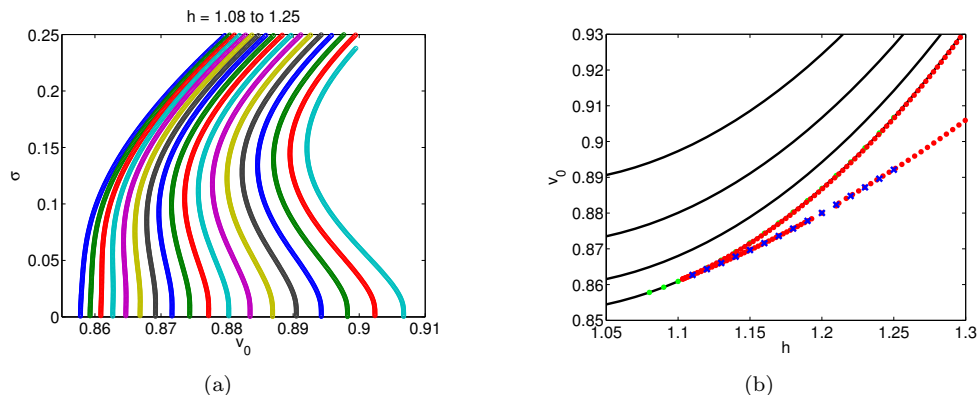


FIG. 6.7. (a) Bifurcation diagrams for $h \in [1.08, 1.25]$, where h increases from the left curve to the right curve. (b) Two-parameter continuation of the fold point in the parameters v_0 and h . The blue crosses mark the points determined from the bifurcation diagrams of the one-parameter continuation, and the red circles are the results from a two-parameter continuation. The black lines show analytical results for the Hopf bifurcation at $\sigma = 0$ (cf. (6.24)). The numerical results for the Hopf bifurcation (zeros from bifurcation diagrams in the left panel) are denoted as green dots; they are in perfect agreement with the analytical results. Note that in the parameter plane projection, the difference between the Hopf and the fold point is barely visible, and the first Hopf curve and the numerical data are obscured by the numerical data for the fold continuation.

real exponent, tangent to the slow manifold that the equation-free approach tries to capture. Floquet vector 2 is shown orthonormalized with respect to Floquet vector 1, because both Floquet vectors 1 and 2 are nearly linearly dependent. While Floquet vector 2 corresponds to a change of amplitude of the shape of the jam, the complex Floquet vectors correspond to spatial perturbations of the jam of low frequency (the spatial frequency is increasing with increasing time frequency and decay rate). When decomposing the perturbation given in Figure 5.4(a) into the eigenbasis, the contribution of the space corresponding to the low-frequency, slow-decay Floquet vectors was small such that one can observe only small-amplitude low-frequency oscillations after the initial rapid decay of all high-frequency strong-decay directions (see inset in Figure 5.4(b)).

These results explain the oscillations observed in Figure 6.5(a). A perturbation of an equilibrium traffic jam in the directions of the leading Floquet vectors is shown in Figure 6.5(b). Small-scale oscillations are visible in the macroscopic trajectories. These oscillations lead to additional oscillations in Figure 6.5(a) after an initial rapid exponential decay of the error. Consequently, Theorem 3.1 is, strictly-speaking, valid only up to a small residual, which in our system is much smaller than the overall dynamics. Thus, the equation-free approach is applicable (and implicit schemes have smaller error than explicit ones) even if the conditions of Theorem 3.1 are not met.

6.3. Continuation of the fold in two parameters. A two-parameter scan, showing one-parameter bifurcation diagrams in the velocity parameter v_0 for different values of the safety distance h , is presented in Figure 6.7(a). The curve of folds as a result of two-parameter continuation in Figure 6.7(a) shows how the fold merges with another saddle-node point in a cusp. The system of equations for continuation of the

fold is [25]

$$\begin{aligned}
F(\sigma, v_0, h) &= 0 \\
F_\sigma(\sigma, v_0, h) &= 0 \\
w^{(\sigma)}(\sigma - \hat{\sigma}) + w^{(v_0)}(v_0 - \hat{v}_0) + w^{(h)}(h - \hat{h}) &= 0
\end{aligned} \tag{6.19}$$

with the Jacobian

$$J = \begin{pmatrix} F_\sigma & F_{v_0} & F_h \\ F_{\sigma\sigma} & F_{v_0\sigma} & F_{h\sigma} \\ w^{(\sigma)} & w^{(v_0)} & w^{(h)} \end{pmatrix}. \tag{6.20}$$

Since derivatives of second order are needed, we apply an approximation of second-order accuracy for the derivatives, i.e., centered differences for the parameter derivatives in v_0 and h and one-sided second-order schemes for derivatives in σ . We use the one-sided second-order approximation for F_σ , because σ is nonnegative by definition. Details for the numerical evaluation of the derivatives can be found in Appendix C.

During the two-parameter continuation the Newton iteration used full Newton steps ($\nu = 1$ in (6.9)). Panel (b) of Figure 6.7 shows the results; they are in perfect agreement with the data obtained by a one-parameter continuation. For comparison we have included the Hopf bifurcation point of the full microscopic system at $\sigma = 0$. The Hopf bifurcation is a pitchfork bifurcation at the macroscopic level. However, since the standard deviation as macroscopic measure is nonnegative by definition, it shows only the nonnegative branches. The analytic expression for the Hopf bifurcation parameter can be found by linearizing system (5.3) around the uniform flow and using the ansatz $(x_n(t), y_n(t)) = (x_n(0) \exp(i\omega t), y_n(0) \exp(i\omega t))$. This results in the system

$$i\omega x_n = y_n \tag{6.21}$$

$$i\omega y_n = \tau^{-1} \left[V' \left(\frac{L}{N} \right) (x_{n+1} - x_n) - y_n \right], \tag{6.22}$$

where ω is the frequency and $V'(\frac{L}{N})$ the first derivative of the optimal velocity function at equilibrium. Eliminating x_n and using the periodic boundary conditions results in

$$\left(1 - \frac{\omega^2 \tau}{V'(\frac{L}{N})} + \frac{i\omega}{V'(\frac{L}{N})} \right)^N = 1. \tag{6.23}$$

This implicitly defines v_0 as a function of h (through V) and can be solved for our specific choice of V (see (5.4)) to yield

$$v_0 = \frac{1 - \cos(2\pi j/N)}{\tau \sin^2(2\pi j/N) (1 - \tanh^2(h - \frac{L}{N}))}, \tag{6.24}$$

where $j = \{1, 2, \dots, N-1\}$. The Hopf curves for the first four spatial frequencies ($j = 1, 2, 3, 4$) are shown in Figure 6.7(b). The analytical results for the first Hopf curve are in perfect agreement with the numerical data. Note that the curves for the Hopf bifurcation point and the fold point are close to each other in the parameter plane shown in Figure 6.7(b).

7. Conclusion and Outlook. In this paper we have derived an implicit method for equation-free analysis and proved its convergence for slow-fast systems with transversally stable slow manifolds. We gave a demonstration by performing an equation-free bifurcation analysis on a one-dimensional macroscopic description emerging from a microscopic traffic model based on a deterministic optimal velocity model for individual drivers. We demonstrated that the obtained bifurcation diagrams are independent of the lifting operator and the healing time in a suitable region. The bifurcation diagram shows a saddle-node bifurcation, which is continued in a two-parameter equation-free pseudoarclength continuation. Since the Hopf bifurcation, i.e., the macroscopic pitch fork, is known analytically, this traffic model is an ideal test case for comparison with new numerical methods. The stability in Figure 6.1 changes at $(v_0, \sigma) = (0.887, 0)$, i.e., sign change of the eigenvalue, indicating a bifurcation. In general, a sufficient characterization would require checking higher-order derivatives of the macroscopic right-hand-side F , which can be numerically demanding in an equation-free computation. A detailed study of the application of the presented implicit equation-free methods to study pitch-fork bifurcations is a possible research direction for future work.

The proof of convergence for the implicit coarse-level time stepper assumes that the slow manifold is transversally stable. The review [13] lists the senses in which a fast high-dimensional chaotic or stochastic system converging in the mean can be viewed as a slow-fast system converging to its slow manifold. In practical applications the result from Section 3.1 may be used as a plausibility check: the equation-free methodology of Kevrekidis *et al* appeals to the notions of singular perturbation theory (cf. the illustrative example in [24]). For any particular system under study, one can check whether this intuition is indeed justified by testing whether the results for the implicit time stepper given by (2.3) are indeed independent of the lifting \mathcal{L} and the healing time t_{skip} if one varies both gradually. For example, Barkley, Kevrekidis and Stuart [2] show that moment maps for simple stochastic or chaotic systems violate this principle in certain regions of their phase space.

For the traffic problems studied in our paper, one long-standing problem is the motion of several phantom jams, i.e., multipulse solutions, relative to each other. For a large number of cars (including the $N = 60$ cars we used) this motion is very slow and therefore near impossible to observe in direct numerical simulations (a phenomenon that is called meta-stability). An open question is whether one can derive a computable criterion that predicts, for a given configuration of several jams and given driver parameters, which of those will collapse or merge and when. This criterion might be based on the shape of the traveling wave. One particularly appealing feature of equation-free analysis is that one can continue macroscopic equilibria in N , the number of cars, using the microscopic model. The complexity of the implicit scheme is independent of N . The increase of computational time is determined by the cost of the microscopic simulation with increasing N , since each function evaluation will be more costly (in our case, proportional to N). Hence, the computational complexity of the overall scheme is proportional to N .

Models closer to situations of practical interest, say with more realistic optimal velocity functions, randomly assigned driver behavior parameters, an element of randomness in the driver behavior, or multiple lanes, as discussed in the literature [17, 29, 31], are also amenable to equation-free analysis. This should provide additional information to help match parameters of macroscopic models to microscopic driver and road parameters.

Acknowledgments. J. Starke and R. Berkemer thank Toyota CRDL for financial support. J. Starke would also like to thank the Danish Research Council FTP under the project number 09-065890/FTP and the Villum Fonden under the VKR-Centre of Excellence 'Ocean Life' for financial support. The research of J. Sieber is supported by EPSRC grant EP/J010820/1.

Appendix A. Proof of Theorem 3.1. For the proof of Theorem 3.1 we have to analyze the two equations (for y and y_* , respectively)

$$\mathcal{R}(M_\varepsilon(t_{\text{skip}}; \mathcal{L}(y))) = \mathcal{R}(M_\varepsilon(t_{\text{skip}} + \delta; \mathcal{L}(x))), \quad (\text{A.1})$$

$$\mathcal{R}(M_\varepsilon(t_{\text{skip}}; g_\varepsilon(\mathcal{L}(y_*)))) = \mathcal{R}(M_\varepsilon(t_{\text{skip}} + \delta; g_\varepsilon(\mathcal{L}(x)))). \quad (\text{A.2})$$

In both equations $x \in \mathbb{R}^d$ enters as a parameter. For (A.2) we have established already in Section 3 that there exists a solution y_* , and that it is locally unique. Equations (3.13) and (3.14) gave a procedure for picking y_* in a globally unique way by starting with $y_* = x$ for $\delta = 0$ and then extending the solution for varying δ until one reaches the desired value of δ . This procedure achieves unique solvability for y_* for all $x \in \text{dom } \mathcal{L}$ and for $t_{\text{skip}} \in [t_0, T_{\text{up}}/\varepsilon)$ and $\delta \geq 0$ satisfying $t_{\text{skip}} + \delta < T_{\text{up}}/\varepsilon$. For equation (A.1) we have to prove the existence of a solution y , and prove that it is close to y_* (including all derivatives with respect to x up to order k).

In order to do this, we need to make the consequences of Fenichel's Theorem more explicit. The Fenichel result (3.4) implies that the map (\mathcal{U} is the neighborhood of \mathcal{C}_0 , which also contains \mathcal{C}_ε)

$$\mathcal{F}_\varepsilon : \mathbb{R} \times \mathcal{U} \ni (\tau, u) \mapsto M_\varepsilon(\tau/\varepsilon; g_\varepsilon(u))$$

is well defined and k times differentiable for all $u \in \mathcal{U}$ and all $\tau \in \mathbb{R}$. This map \mathcal{F}_ε is the flow map when restricted to the slow manifold \mathcal{C}_ε , and projects all points in the neighborhood of the slow manifold \mathcal{C}_ε along the stable fibers using g_ε . Note that τ is the time on the *slow* time scale as we divide by ε in the evaluation of the map. The derivatives of \mathcal{F}_ε with respect to its second argument u are uniformly bounded for all $u \in \mathcal{U}$ as long as $\tau \in [0, T_{\text{up}}]$:

$$\|\partial_2^j \mathcal{F}_\varepsilon(\tau; \cdot)\| \leq C, \quad (j = 0 \dots, k, \text{ and } \tau \in [0, T_{\text{up}}]). \quad (\text{A.3})$$

Correspondingly, the map

$$A_\varepsilon(\tau; \cdot) = \mathcal{R}(\mathcal{F}_\varepsilon(\tau; \mathcal{L}(\cdot))) : \text{dom } \mathcal{L} \ni x \mapsto \mathcal{R}(M_\varepsilon(\tau/\varepsilon; g_\varepsilon(\mathcal{L}(x)))) \quad (\text{A.4})$$

is well defined for all $\tau \in \mathbb{R}$ and locally invertible for all $\varepsilon \in [0, \varepsilon_0)$ and τ satisfying $|\tau| < T_{\text{up}}$. Note that the range of admissible ε includes $\varepsilon = 0$, because the limit of the right-hand side of (A.4) for $\varepsilon = 0$ is well defined as the solution of a differential-algebraic equation on \mathcal{C}_0 on the slow time scale. The norms of the derivatives of A_ε and its (locally unique) inverse can be bounded by a uniform constant C independent of $\varepsilon \in [0, \varepsilon_0)$ and τ as long as $|\tau| \leq T_{\text{up}}$:

$$\|\partial_2^j A_\varepsilon(\tau; \cdot)\| \leq C, \quad \|\partial_2^j A_\varepsilon^{-1}(\tau; \cdot)\| \leq C. \quad (\text{A.5})$$

Similarly, the motion transversal to the slow manifold \mathcal{C}_ε consists of a fast decay and a slow tracking of the dynamics on \mathcal{C}_ε . Let $K < K_0$ be a given contraction rate, and choose the upper bound ε_0 such that the contraction property (3.5) of the stable fiber

projection g_ε holds for all $\varepsilon < \varepsilon_0$ and all $u \in \mathcal{U}$. Then we can express the transversal component of the flow starting from an arbitrary $u \in \mathcal{U}$ and $t \geq 0$ in the form

$$M_\varepsilon(t; u) = M_\varepsilon(t; g_\varepsilon(u)) + \exp(-Kt)M_\varepsilon^\perp(t; u) \quad (\text{A.6})$$

(this defines M_ε^\perp). In the right-hand side of (A.6) the map M_ε^\perp is k times differentiable with respect to its argument u for all $\varepsilon \in [0, \varepsilon_0)$ (including $\varepsilon = 0$), and the norms of $M_\varepsilon^\perp(t; u)$ and its partial derivatives $\partial^j M_\varepsilon^\perp(t; u)$ are uniformly bounded for all $t \in [0, \infty)$, $\varepsilon \in [0, \varepsilon_0)$ and $u \in \mathcal{U}$:

$$\|M_\varepsilon^\perp(t; x)\| \leq C, \quad \|\partial_2^j M_\varepsilon^\perp(t; x)\| \leq C. \quad (\text{A.7})$$

The prefactor $\exp(-Kt)$ can also be extracted if the smooth restriction map \mathcal{R} is applied to both terms on the left-hand side of (A.6), and if we insert $\mathcal{L}(x)$ for u . Thus,

$$\mathcal{R}(M_\varepsilon(t; \mathcal{L}(x))) - \mathcal{R}(M_\varepsilon(t; g_\varepsilon(\mathcal{L}(x)))) \quad (\text{A.8})$$

$$= \int_0^1 \partial \mathcal{R} \left(M_\varepsilon(t; g_\varepsilon(\mathcal{L}(x))) + \rho [M_\varepsilon(t; \mathcal{L}(x)) - M_\varepsilon(t; g_\varepsilon(\mathcal{L}(x)))] \right) d\rho \quad (\text{A.9})$$

$$\times [M_\varepsilon(t; \mathcal{L}(x)) - M_\varepsilon(t; g_\varepsilon(\mathcal{L}(x)))]$$

$$= \int_0^1 \partial \mathcal{R} \left(\mathcal{F}_\varepsilon(\varepsilon t; \mathcal{L}(x)) + \rho \exp(-Kt) M_\varepsilon^\perp(t; \mathcal{L}(x)) \right) d\rho \exp(-Kt) M_\varepsilon^\perp(t; \mathcal{L}(x)). \quad (\text{A.10})$$

We applied the mean-value theorem to equate (A.8) and (A.9). To get to the right-hand side of (A.10), we inserted the representation (A.6) and used the definition of the map \mathcal{F}_ε . This right-hand side in (A.10) has the form

$$\text{right-hand side of (A.10)} = \exp(-Kt) r_\varepsilon(\varepsilon t, t; x), \quad (\text{A.11})$$

where the first argument of r_ε refers to the time dependence of A_ε in the argument of $\partial \mathcal{R}$. Note that we have introduced the slow time scale as an additional argument into r_ε . We will consider $r_\varepsilon(\tau, t; x)$ for arbitrary $\tau \in [0, T_{\text{up}}]$ and $t \in [0, \infty)$ below, and later insert $\tau = \varepsilon t$ as a particular case. The map $r_\varepsilon(\tau, t; x)$ is k times continuously differentiable with respect to x . The norm of r_ε and the norm of its derivatives with respect to x are uniformly bounded for $x \in \text{dom } \mathcal{L}$, $\varepsilon \in [0, \varepsilon_0)$, $\tau \in [0, T_{\text{up}}]$, and $t \in [0, \infty)$ because all of its ingredients have bounded derivatives (listed in (A.3), (A.7)):

$$\|r_\varepsilon(\tau, t; x)\| \leq C, \quad \|\partial_3^j r_\varepsilon(\tau, t; x)\| \leq C \quad (\text{A.12})$$

for $j \in \{1, \dots, k\}$. Let us define the times corresponding to t_{skip} and δ on the slow time scale as:

$$\tau_{\text{skip}} = \varepsilon t_{\text{skip}}, \quad \Delta = \varepsilon \delta. \quad (\text{A.13})$$

If τ_{skip} and $\tau_{\text{skip}} + \Delta$ are in $[0, T_{\text{up}}]$, then the solution y_* of the exact flow satisfies (using the locally invertible map A_ε defined in (A.4))

$$A_\varepsilon(\tau_{\text{skip}}; y_*) = A_\varepsilon(\tau_{\text{skip}} + \Delta; x). \quad (\text{A.14})$$

Using r_ε and A_ε , equation (A.1) can be rewritten as

$$A_\varepsilon(\tau_{\text{skip}}; y) + s_1 r_\varepsilon(\tau_{\text{skip}}, t_1; y) = A_\varepsilon(\tau_{\text{skip}} + \Delta; x) + s_2 r_\varepsilon(\tau_{\text{skip}} + \Delta, t_2; x), \quad (\text{A.15})$$

where

$$\begin{aligned} s_1 &= \exp(-K t_{\text{skip}}), & s_2 &= \exp(-K(t_{\text{skip}} + \delta)), \\ t_1 &= t_{\text{skip}} \geq 0, & t_2 &= t_{\text{skip}} + \delta \geq 0. \end{aligned} \quad (\text{A.16})$$

We will first consider solvability of (A.15) with respect to y for general s_1 and s_2 close to 0, and $t_1, t_2 \in [0, \infty)$. This solution y will depend on the parameters s_1, s_2, t_1 , and t_2 (among others). Whenever we subsequently insert the particular values from (A.13) and (A.16) for $\tau_{\text{skip}}, \Delta, s_1, s_2, t_1$, and t_2 , the solution y of (A.15) becomes also a solution of (A.1). For each of the terms, $A_\varepsilon, A_\varepsilon^{-1}$, and r_ε , we have uniform upper bounds ((A.5) and (A.12)) for their norms and all derivatives up to order k for the entire range of arguments: $x, y \in \text{dom } \mathcal{L}, \tau_{\text{skip}} \in [0, T_{\text{up}}], \tau_{\text{skip}} + \Delta \in [0, T_{\text{up}}], t_1, t_2 \in [0, \infty)$, and $\varepsilon \in [0, \varepsilon_0)$ (where ε_0 is determined by the choice of decay rate K as given by Fenichel's Theorem). Thus, we can use (A.14) and (A.15) to establish the existence of y and its distance to y_* using the implicit function theorem at the point $s_1 = s_2 = 0$.

The exact solution y_* is a uniformly regular solution of (A.15) for $s_1 = s_2 = 0$, all $x \in \text{dom } \mathcal{L}, \varepsilon \in [0, \varepsilon_0), \tau_{\text{skip}} \in [0, T_{\text{up}}]$, and $\Delta \in [-\tau_{\text{skip}}, T_{\text{up}} - \tau_{\text{skip}}]$. Thus, for small s_1 and s_2 , equation (A.15) has a locally unique solution $y \in \text{dom } \mathcal{L}$ which depends smoothly on all parameters (we write $y(x, s_1, s_2)$ to emphasize the dependence on $(s_1, s_2) \in \mathbb{R}^2$) such that

$$\|\partial_1^j y(x, s_1, s_2) - \partial^j y_*(x)\|_\infty \leq C \|(s_1, s_2)\|_\infty$$

($j \in \{1, \dots, k\}$) for some constant C and all $s_1, s_2 \in (-\rho, \rho)$ for some $\rho > 0$. Consequently, if we choose t_0 such that $\exp(-K t_0) < \rho$ and decrease ε_0 such that $t_0 < T_{\text{up}}/\varepsilon_0$, then we have for all $\varepsilon \in (0, \varepsilon_0), t_{\text{skip}} \in [t_0, T_{\text{up}}/\varepsilon], \delta \in [0, T_{\text{up}}/\varepsilon - t_{\text{skip}}]$, and $x \in \text{dom } \mathcal{L}$ that

$$\begin{aligned} & \left\| \partial_1^j y(x, \exp(-K t_{\text{skip}}), \exp(-K(t_{\text{skip}} + \delta))) - \partial^j y_*(x) \right\|_\infty \\ & \leq C \|(\exp(-K t_{\text{skip}}), \exp(-K(t_{\text{skip}} + \delta)))\|_\infty \\ & \leq C \exp(-K t_{\text{skip}}) \end{aligned}$$

for all $j \in \{1, \dots, k\}$. This establishes the convergence claim of Theorem 3.1 since y is the solution of (A.1) if $s_1 = \exp(-K \tau_{\text{skip}}/\varepsilon) = \exp(-K t_{\text{skip}}), s_2 = \exp(-K(\tau_{\text{skip}} + \Delta)/\varepsilon) = \exp(-K(t_{\text{skip}} + \delta)), t_1 = t_{\text{skip}}, t_2 = t_{\text{skip}} + \delta, \tau_{\text{skip}} = \varepsilon t_{\text{skip}}$, and $\Delta = \varepsilon \delta$.

Appendix B. Parameters. The parameters used for the simulations are listed in Table B.1.

Appendix C. Finite Differences. For the scheme (6.19), F is evaluated at the

Parameter	Value/range
τ^{-1}	1.7
L	60
N	60
μ	0.1
s	0.001
δ	2000
Δt	-5000
t_{skip}	300
v_0^*	0.8, \dots, 1.0
h^*	1.0, \dots, 1.7

TABLE B.1

Parameters for numerical studies. The quantities marked with an asterisk (*) are bifurcation parameters, where the range used is noted

17 points

$$\begin{aligned}
1 : (\sigma, v_0, h), & & 3 : (\sigma + 2\Delta\sigma, v_0, h), \\
2 : (\sigma + \Delta\sigma, v_0, h), & & 4 : (\sigma + 3\Delta\sigma, v_0, h), \\
4 : (\sigma + 3\Delta\sigma, v_0, h), & & 5 : (\sigma + 4\Delta\sigma, v_0, h), \\
6 : (\sigma, v_0 - \Delta v_0, h), & & 7 : (\sigma, v_0 + \Delta v_0, h), \\
8 : (\sigma + \Delta\sigma, v_0 - \Delta v_0, h), & & 9 : (\sigma + \Delta\sigma, v_0 + \Delta v_0, h), \\
10 : (\sigma + 2\Delta\sigma, v_0 - \Delta v_0, h), & & 11 : (\sigma + 2\Delta\sigma, v_0 + \Delta v_0, h), \\
12 : (\sigma, v_0, h - \Delta h), & & 13 : (\sigma, v_0, h + \Delta h), \\
14 : (\sigma + \Delta\sigma, v_0, h - \Delta h), & & 15 : (\sigma + \Delta\sigma, v_0, h + \Delta h), \\
16 : (\sigma + 2\Delta\sigma, v_0, h - \Delta h), & & 17 : (\sigma + 2\Delta\sigma, v_0, h + \Delta h).
\end{aligned} \tag{C.1}$$

where $\Delta\sigma = \Delta v_0 = \Delta h = 0.001$ are offsets for the approximation. One can use the following second-order accuracy scheme to compute the derivatives (for better readability, the points are just referred to by their number, e.g., $F_7 = F(\sigma, v_0 + \Delta v_0, h)$):

$$\begin{aligned}
F_\sigma &= \frac{-3F_1 + 4F_2 - F_3}{2\Delta\sigma} \\
F_{v_0} &= \frac{F_7 - F_6}{2\Delta v_0} \\
F_h &= \frac{F_{13} - F_{12}}{2\Delta h} \\
F_{\sigma\sigma} &= \frac{-3(-3F_1 + 4F_2 - F_3) + 4(-3F_2 + 4F_3 - F_4) - (-3F_3 + 4F_4 - F_5)}{4(\Delta\sigma)^2} \\
F_{v_0\sigma} &= \frac{(-3F_7 + 4F_9 - F_{11}) - (-3F_6 + 4F_8 - F_{10})}{4\Delta\sigma\Delta v_0} \\
F_{h\sigma} &= \frac{(-3F_{13} + 4F_{15} - F_{17}) - (-3F_{12} + 4F_{14} - F_{16})}{4\Delta\sigma\Delta h}
\end{aligned}$$

REFERENCES

- [1] M. BANDO, K. HASEBE, A. NAKAYAMA, A. SHIBATA, AND Y. SUGIYAMA, *Dynamical model of traffic congestion and numerical simulation*, Phys. Rev. E, 51 (1995), pp. 1035–1042.
- [2] D. BARKLEY, I. G. KEVREKIDIS, AND A. M. STUART, *The moment map: nonlinear dynamics of density evolution via a few moments*, SIAM Journal on Applied Dynamical Systems, 5 (2006), pp. 403–434.
- [3] B. P. BELOUSOV, *A periodic reaction and its mechanism*, Collection of short papers on radiation medicine for 1958, (1959).
- [4] L. CHEN, P.G. DEBENEDETTI, C.W. GEAR, AND I.G. KEVREKIDIS, *From molecular dynamics to coarse self-similar solutions: a simple example using equation-free computation*, Journal of Non-Newtonian Fluid Mechanics, 120 (2004), pp. 215 – 223.
- [5] JAIME CISTERNAS, C. WILLIAM GEAR, SIMON LEVIN, AND IOANNIS G. KEVREKIDIS, *Equation-free modelling of evolving diseases: coarse-grained computations with individual-based models*, Proceedings of the Royal Society of London. Series A: Mathematical, Physical and Engineering Sciences, 460 (2004), pp. 2761–2779.
- [6] O. CORRADI, P. HJORTH, AND J. STARKE, *Equation-free detection and continuation of a Hopf bifurcation point in a particle model of pedestrian flow*, SIAM Journal on Applied Dynamical Systems, 11 (2012), pp. 1007–1032.
- [7] W. E AND B. ENQUIST, *Multiscale modeling and computation*, Notices of the AMS, 50 (2003), pp. 1062–1070.
- [8] MICHAEL ELMEGAARD, JAN RUBEL, MIZUHO INAGAKI, ATSUSHI KAWAMOTO, AND JENS STARKE, *Equation-free continuation of maximal vibration amplitudes in a nonlinear rotor-bearing model of a turbocharger*, ASME Conference Proceedings, 2009 (2009), pp. 369–378.
- [9] N. FENICHEL, *Geometric singular perturbation theory for ordinary differential equations*, Journal of Differential Equations, 31 (1979), pp. 53–98.
- [10] YU B. GAIDIDEI, R. BERKEMER, J. G. CAPUTO, P. L. CHRISTIANSEN, A. KAWAMOTO, T. SHIGA, M. P. SORENSEN, AND J. STARKE, *Analytical solutions of jam pattern formation on a ring for a class of optimal velocity traffic models*, New J. Phys., 11 (2009), p. 073012.
- [11] I. GASSER, G. SIRITO, AND B. WERNER, *Bifurcation analysis of a class of ‘car following’ traffic models*, Physica D: Nonlinear Phenomena, 197 (2004), pp. 222 – 241.
- [12] C. W. GEAR, T. J. KAPER, I. G. KEVREKIDIS, AND A. ZAGARIS, *Projecting to a slow manifold: Singularly perturbed systems and legacy codes*, SIAM Journal on Applied Dynamical Systems, 4 (2005), pp. 711–732.
- [13] DROR GIVON, RAZ KUPFERMAN, AND ANDREW STUART, *Extracting macroscopic dynamics: model problems and algorithms*, Nonlinearity, 17 (2004), pp. 55–127.
- [14] T. GROSS AND I. G. KEVREKIDIS, *Robust oscillations in SIS epidemics on adaptive networks: Coarse graining by automated moment closure*, Europhysics Letters, 82 (2008), p. 38004.
- [15] H. HAKEN, *Advanced synergetics. Instability hierarchies of self-organizing systems and devices / Springer series in synergetics 20*, Springer, Berlin, 1983.
- [16] ———, *Synergetics. An introduction. Nonequilibrium phase transitions and self organization in physics, chemistry and biology. 3.ed / Springer series in synergetics 1*, Springer, Berlin, 1983.
- [17] DIRK HELBING, *Traffic and related self-driven many-particle systems*, Rev. Mod. Phys., 73 (2001), pp. 1067–1141.
- [18] [HTTP://WWW.MATHWORKS.COM](http://www.mathworks.com), MATLAB R2011B, 64-bit (glnxa64).
- [19] MASAHIRO KANAI, KATSUHIRO NISHINARI, AND TETSUJI TOKIHIRO, *A stochastic optimal velocity model and its long-lived metastability*, Physical Review E, 72 (2009), p. 035102.
- [20] AL KELLEY, *The stable, center-stable, center, center-unstable, unstable manifolds*, Journal of Differential Equations, 3 (1967), pp. 546 – 570.
- [21] IOANNIS G. KEVREKIDIS, C. WILLIAM GEAR, AND GERHARD HUMMER, *Equation-free: The computer-aided analysis of complex multiscale systems*, AIChE Journal, 50 (2004), pp. 1346–1355.
- [22] IOANNIS G. KEVREKIDIS, C. WILLIAM GEAR, JAMES M. HYMAN, PANAGIOTIS G. KEVREKIDIS, OLOF RUNBORG, AND CONSTANTINOS THEODOROPOULOS, *Equation-free, coarse-grained multiscale computation: enabling microscopic simulators to perform system-level analysis*, Communications in Mathematical Sciences, 1 (2003), pp. 715 – 762.
- [23] IOANNIS G. KEVREKIDIS AND GIOVANNI SAMAIEY, *Equation-free multiscale computation: Algorithms and applications*, Annual Review of Physical Chemistry, 60 (2009), pp. 321–344.
- [24] Y. KEVREKIDIS AND G. SAMAIEY, *Equation-free modeling*, Scholarpedia, 5 (2010), p. 4847.
- [25] YURI A. KUZNETSOV, *Elements of Applied Bifurcation Theory*, vol. 112 of Applied Mathematical Sciences, Springer, New York, third ed., 2004.
- [26] CARLO LAING, *On the application of ‘equation-free modelling’ to neural systems*, Journal of Computational Neuroscience, 20 (2006), pp. 5–23.

- [27] JU LI, PANAYOTIS G. KEVREKIDIS, C. WILLIAM GEAR, AND IOANNIS G. KEVREKIDIS, *Deciding the nature of the coarse equation through microscopic simulations: The baby-bathwater scheme*, Multiscale Modeling & Simulation, 1 (2003), pp. 391–407.
- [28] ALEXEI G. MAKEEV, DIMITRIOS MAROUDAS, ATHANASSIOS Z. PANAGIOTOPOULOS, AND IOANNIS G. KEVREKIDIS, *Coarse bifurcation analysis of kinetic Monte Carlo simulations: A lattice-gas model with lateral interactions*, The Journal of Chemical Physics, 117 (2002), pp. 8229–8240.
- [29] TAKASHI NAGATANI, *The physics of traffic jams*, Reports on Progress in Physics, 65 (2002), p. 1331.
- [30] GABOR OROSZ, BERND KRAUSKOPF, AND R. EDDIE WILSON, *Bifurcations and multiple traffic jams in a car-following model with reaction-time delay*, Physica D: Nonlinear Phenomena, 211 (2005), pp. 277 – 293.
- [31] GABOR OROSZ, R. EDDIE WILSON, AND GABOR STEPAN, *Traffic jams: dynamics and control*, Philosophical Transactions of the Royal Society A: Mathematical, Physical and Engineering Sciences, 368 (2010), pp. 4455–4479.
- [32] LORD RAYLEIGH, *On convection currents in a horizontal layer of fluid, when the higher temperature is on the under side*, Phil. Mag., Ser.6, 32 (1916), pp. 529 – 546.
- [33] ANDREAS I. REPPAS, ANDREAS C. TSOUMANIS, AND CONSTANTINOS I. SIETTOS, *Coarse-grained bifurcation analysis and detection of criticalities of an individual-based epidemiological network model with infection control*, Applied Mathematical Modelling, 34 (2010), pp. 552 – 560.
- [34] E. SANCHEZ-PALENCIA, *Homogenization method for the study of composite media*, in Asymptotic Analysis II, F. Verhulst, ed., vol. 985 of Lecture Notes in Mathematics, Springer Berlin Heidelberg, 1983, pp. 192–214.
- [35] KEIZO SHIGAKI, JUN TANIMOTO, AND AYA HAGISHIMA, *A revised stochastic optimal velocity model considering the velocity gap with a preceding vehicle*, Int. J. Mod. Phys. C, 22 (2011), pp. 1005–1014.
- [36] C. I. SIETTOS, A. ARMAOU, A. G. MAKEEV, AND I. G. KEVREKIDIS, *Microscopic/stochastic timesteppers and ‘coarse’ control: A KMC example*, AIChE Journal, 49 (2003), pp. 1922–1926.
- [37] C. I. SIETTOS, M. D. GRAHAM, AND I. G. KEVREKIDIS, *Coarse Brownian dynamics for nematic liquid crystals: Bifurcation, projective integration, and control via stochastic simulation*, The Journal of Chemical Physics, 118 (2003), pp. 10149–10156.
- [38] HERBERT SPOHN, *Large scale dynamics of interacting particles*, Texts and Monographs in Physics, Springer-Verlag, 1991.
- [39] CHRISTOPHE VANDEKERCKHOVE, BENJAMIN SONDAY, ALEXEI MAKEEV, DIRK ROOSE, AND IOANNIS G. KEVREKIDIS, *A common approach to the computation of coarse-scale steady states and to consistent initialization on a slow manifold*, Computers & Chemical Engineering, 35 (2011), pp. 1949 – 1958.
- [40] A. VANDERBAUWHUDE, *Center manifolds, normal forms and elementary bifurcations*, Dynamics Reported, 2 (1989).
- [41] DAVID A. YOUNG, *A local activator-inhibitor model of vertebrate skin patterns*, Mathematical Biosciences, 72 (1984), pp. 51 – 58.
- [42] ANTONIOS ZAGARIS, C. WILLIAM GEAR, TASSO J. KAPER, AND YANNIS G. KEVREKIDIS, *Analysis of the accuracy and convergence of equation-free projection to a slow manifold*, ESAIM: Mathematical Modelling and Numerical Analysis, 43 (2009), pp. 757–784.
- [43] A. ZAGARIS, C. VANDEKERCKHOVE, C. W. GEAR, T. J. KAPER, AND I. G. KEVREKIDIS, *Stability and stabilization of the constrained runs schemes for equation-free projection to a slow manifold*, Discrete and Continuous Dynamical Systems - Series A, 32 (2012), pp. 2759 – 2803.
- [44] A. M. ZHABOTINSKY, *Periodical oxidation of malonic acid in solution (a study of the Belousov reaction kinetics)*, Biofizika, 9 (1964), pp. 306–11.